Cirrus cloud thinning using a more physically-based ice microphysics scheme in the ECHAM-HAM GCM

Colin Tully , David Neubauer , Nadja Omanovic , and Ulrike Lohmann

Institute for Climate and Atmospheric Science, ETH Zurich, Zurich, Switzerland

Correspondence: Colin Tully (colin.tully@env.ethz.ch)

Abstract. Cirrus cloud thinning (CCT) is a relatively new radiation management proposal to counteract anthropogenic climate warming by targeting Earth's terrestrial radiation balance. The efficacy of this method was presented in several general circulation model (GCM) studies that showed widely varied radiative responses, originating in part from the differences in the representation of cirrus ice microphysics between the different GCMs. The recent implementation of a new, more physically-

5   based ice microphysics scheme (Predicted Particle Properties, P3) that abandons ice hydrometeor size class separation into the ECHAM-HAM GCM, coupled to a new approach for calculating cloud fractions that increases the relative humidity (RH) thresholds for cirrus cloud formation, motivated a reassessment of CCT efficacy. In this study, we first compared CCT sensitivity between the new cloud fraction approach and the original ECHAM-HAM cloud fraction approach. With the P3 scheme and the higher RH thresholds for cirrus cloud formation, we find a significant cooling response of $-0.36\,\mathrm{W\,m^{-2}}$ only for our

10   simulation with a seeding particle concentration of $1\,\mathrm{L^{-1}}$, due mostly to rapid cloud adjustments. The most notable response is the reduction of the maximum global-mean net top-of-atmosphere (TOA) radiative anomalies from overseeding by more than $50\,\%$, from $9.0\,\mathrm{W\,m^{-2}}$ with the original cloud fraction approach, down to $4.3\,\mathrm{W\,m^{-2}}$ using the new cloud fraction RH thresholds by avoiding artificial ice-cloud expansion upon ice nucleation. We attribute the large positive TOA anomalies to seeding particles overtaking both homogeneous nucleation and heterogeneous nucleation on mineral dust particles within cirrus clouds

15   to produce more numerous and smaller ice crystals. This effect is amplified by longer ice residence times in clouds due to the more realistic, slower removal of ice via sedimentation in the P3 scheme. In an effort to avoid this overtaking effect of seeding particles, we increased the default critical ice saturation ratio ($S_{i,seed}$) for ice nucleation on seeding particles from the default value of 1.05 to 1.35 in a second sensitivity test. With the higher $S_{i,seed}$ we eliminate overseeding and are able to produce cooling responses over a broader range of seeding particle concentrations, with the largest cooling of $-0.32\,\mathrm{W\,m^{-2}}$ for a seeding

20   particle concentration of $10\,\mathrm{L^{-1}}$, which suggests that $S_{i,seed}$ is a key factor to consider for future CCT studies. However, the global-mean TOA anomalies contain high uncertainty. In response, we examined the TOA responses regionally and found that specific regions only show a small potential for targeted CCT, which is partially enhanced by using the larger $S_{i,seed}$. Finally, in a seasonal analysis of TOA responses to CCT, we find that our results do not support the previous finding that high-latitude wintertime seeding is a feasible strategy to enhance CCT efficacy, as seeding in our model enhances the already positive cirrus

25   longwave cloud radiative effect. Instead our results show that summertime cooling occurs due to adjustments of lower-lying mixed-phase and liquid clouds. Therefore, we conclude that CCT is unlikely to act as a feasible climate intervention strategy

on a global scale, and should be investigated further with higher-resolution studies in potential target regions and with studies dedicated to assessing potentially realistic seeding particle materials.

1 Introduction

Limiting 21st Century global average warming to within $2\,°C$, following the 2015 Paris Climate Agreement, through greenhouse gas emissions reduction alone remains a highly ambitious goal. Amid growing concern of this infeasibility, several climate intervention (CI, also referred to as climate engineering or geoengineering) methods were proposed as potential mitigation strategies in order to limit future warming (Vaughan and Lenton, 2011). CI strategies encompass carbon sequestration, which targets one of the main drivers of anthropogenic climate change, namely increased atmospheric CO_2 concentrations, and radiation management (RM), which indirectly counteracts warming by altering Earth's radiation balance. These RM schemes can be further divided between solar, shortwave (SW) and terrestrial, longwave (LW) radiation strategies. The focus of this study is on one particular LW radiation strategy, cirrus cloud thinning (CCT), also referred to as cirrus seeding, that aims to increase the amount of outgoing LW radiation to space by altering the formation pathways of cirrus clouds using artificial ice nucleating particles (INPs).

Cirrus clouds are found in the upper troposphere at temperatures below $238\,K$ (cirrus regime) and as such consist entirely of ice crystals. Unlike their lower-altitude mixed-phase or liquid counterparts, cirrus clouds possess a relatively weak SW albedo effect while significantly modulating outgoing LW radiation. They absorb LW radiation emitted at warmer temperatures from Earth's surface and the lower-lying atmosphere, and re-emit it at low temperatures, resulting in a top-of-atmosphere (TOA) "trapping" effect that warms the atmosphere below (Hong et al., 2016; Gasparini et al., 2020). However, the magnitude of this cloud radiative effect (CRE) of cirrus clouds is strongly influenced by the microphysical properties of the clouds, the ice crystal number concentration (ICNC) and their sizes, which are determined by the ice formation pathways (Stephens et al., 1990; DeMott et al., 2003, 2010; Krämer et al., 2016; Heymsfield et al., 2017).

Ice formation in cirrus occurs via two modes: homogeneous and heterogeneous nucleation. The former occurs as the spontaneous freezing of aqueous solution droplets at a relative humidity with respect to ice between $150\,\%$ and $170\,\%$ (Koop et al., 2000; Kärcher and Lohmann, 2002; Heymsfield et al., 2017) in the absence of a surface for ice nucleation. Due to the stochastic nature of a homogeneous nucleation event, numerous ice particles can form (Krämer et al., 2016; Heymsfield et al., 2017; Gasparini et al., 2018) that are limited in size due to their competition for the available water vapor (Ickes et al., 2015). The resulting cirrus ICNC, however, is sensitive to the appropriate conditions, namely the updraft speed that determines the magnitude of ice supersaturation (Kärcher and Lohmann, 2002; Lohmann and Kärcher, 2002; Kärcher et al., 2006; Kuebbeler et al., 2014; Jensen et al., 2016b).

Heterogeneous ice nucleation occurs on the surface of a solid aerosol particle called an INP. The availability of the INP surface lowers the energy barrier for ice germ formation, allowing ice nucleation at lower ice supersaturations and higher temperatures than homogeneous freezing. However, understanding how heterogeneous nucleation impacts cirrus cloud properties

60 is complicated by the fact that several mechanisms exist for ice formation via an INP (Heymsfield et al., 2017). Plus, only a small fraction of aerosols acts as INPs, which are even more sparsely populated in the upper troposphere, with limited measurements in the cirrus regime (DeMott et al., 2003, 2010; Cziczo et al., 2013). Significant research continues on the ability of various materials (e.g. mineral dust (Möhler et al., 2008; Lohmann et al., 2008; Murray et al., 2012; Ullrich et al., 2017), and aircraft soot (Mahrt et al., 2018, 2020; Lohmann et al., 2020)) to act as INPs (Kanji et al., 2017).

65 The differences in the ice formation pathways via the two nucleation modes can result in cirrus clouds with different properties (Krämer et al., 2016; Heymsfield et al., 2017; Gasparini et al., 2018). While homogeneous nucleation tends to form numerous small ice crystals, the number of ice particles formed by heterogeneous nucleation is dependent on the availability of INPs, especially in the case of slow updrafts (Kärcher and Lohmann, 2003; Spichtinger and Cziczo, 2010). In the case of stronger updrafts or in an environment with a low INP concentration, heterogeneous nucleation is less effective as water vapor

70 consumption may not be sufficient to diminish the updraft-fueled supersaturation increase (DeMott et al., 2010; Jensen et al., 2016b). Krämer et al. (2016) and Gasparini et al. (2018) reported noticeable differences in the ice water content (IWC) of cirrus formed directly from the gas phase ("in-situ") via the two nucleation modes, with heterogeneously-formed cirrus associated with having lower IWC and smaller ICNC than homogeneously-formed cirrus. Differences are also evident in ice particle sizes, which are indirectly related to the ICNC, with fewer particles being larger in heterogeneously-formed cirrus than numerous

75 small particles in homogeneously-formed cirrus (Heymsfield et al., 2017). DeMott et al. (2010) found that the smaller ice particles formed by homogeneous nucleation form cirrus clouds at higher altitudes (i.e. colder temperatures), contributing to a stronger warming effect. The fewer and larger ice particles formed on INPs result in lower and warmer cirrus that have a weaker warming effect. The differences in radiative effects between the ice nucleation modes was also assessed by Lohmann et al. (2008) with the ECHAM general circulation model (GCM). In a series of sensitivity tests they found that switching cirrus

80 ice nucleation from homogeneous only to purely heterogeneous nucleation reduced the net cloud radiative forcing by roughly $2\,\mathrm{W\,m^{-2}}$. A similar response was found when a simplified simulation of competition between the two nucleation modes in the cirrus regime was included. The responses can be explained through changes in ice crystal fall speeds, which are closely related to nucleation rates that determine the initial size of the ice crystals (Mitchell et al., 2008). Following these findings, Mitchell and Finnegan (2009) were the first to propose using efficient artificial INPs (i.e. "seeding particles") to alter cirrus ice

85 environments away from small ice particles formed via homogeneous nucleation to predominantly larger ice particles formed via heterogeneous nucleation that sediment quicker and reduce cirrus cloud lifetimes, following a process coined as the negative Twomey effect (Kärcher and Lohmann, 2003). In the preliminary analysis by Mitchell and Finnegan (2009), they proposed CCT could have a cooling potential of more than $-2.8\,\mathrm{W\,m^{-2}}$ that could noticeably counteract warming from a doubling of CO_2.

90 Natural nucleation competition in cirrus was excluded in the first GCM CCT study by Storelvmo et al. (2013), who assumed all cirrus formed via homogeneous nucleation in the CAM5 general circulation model (GCM). Globally uniform seeding

produced a maximum negative net ΔCRE around $-2.0\,\mathrm{Wm^{-2}}$, corresponding to optically thinner cirrus with an average ice crystal effective radius increase of $4\,\mu\mathrm{m}$ and decrease of ICNC by more than $250\,\mathrm{L^{-1}}$. Of note from their study was evidence of an optimal seeding particle concentration around $18\,\mathrm{L^{-1}}$, below which the seeding particles were ineffective due to insufficient
95 water vapor consumption. However, a seeding concentration above the optimal concentration led to "overseeding", whereby the numerous seeding INPs formed smaller ice particles that elongated cirrus lifetimes and exerted a warming effect (Storelvmo et al., 2013).

The assumption that cirrus form primarily by homogeneous nucleation was challenged when Cziczo et al. (2013) observed heterogeneous nucleation as the dominant source of cirrus ice over North and Central America. To account for the uncertainty
100 surrounding the dominant ice nucleation mode in cirrus, Storelvmo and Herger (2014) conducted several seeding simulations with different configurations of ice nucleation competition, including different concentrations of background dust as active INPs. They found a reduced CRE response up to $-2\,\mathrm{Wm^{-2}}$ in their simulations where seeding particles were added to homogeneous-heterogeneous nucleation competition and homogeneous-only configurations, with an optimal seeding particle concentration of $18\,\mathrm{L^{-1}}$ as in Storelvmo et al. (2013). Additionally, they found that seeding at this optimal concentration in
105 their model led to optically thinner clouds that contained a weaker overall SW CRE (i.e. reduced albedo), allowing more SW to reach the surface. However, this effect was outweighed by the reduction in cirrus LW CRE (i.e. reduced LW "trapping"). To some extent, this finding is in line with the latest compilation of in-situ observations of unseeded cirrus by Krämer et al. (2020), who found that optically thicker, liquid-origin, cirrus (cloud optical depth, $\tau > 1$) tend to have a strong cooling effect due to a higher albedo, whereas optically thinner, in-situ origin, cirrus ($\tau < 1$) have a large warming effect in response to a weaker
110 albedo and a larger LW-trapping potential (i.e. cooler temperatures) that peaks with τ between 0.4 and 0.5. Krämer et al. (2020) further divide in-situ origin cirrus between fast and slow updrafts, with the latter having a stronger warming potential than the former. As CCT targets the slower updraft cirrus, due to weaker dynamic forcing (Gasparini et al., 2017; Krämer et al., 2016; Krämer et al., 2020), thinning these cirrus weakens their warming potential. Therefore, reducing the optical thickness of these latter cirrus through seeding, like in Storelvmo and Herger (2014), not only reduces their already weak SW CRE, but
115 reduces their LW CRE more effectively. At higher seeding particle concentrations and for their heterogeneous-only simulation, Storelvmo and Herger (2014) found warming of more than $1.0\,\mathrm{Wm^{-2}}$ as a result of overseeding. They also showed that non-uniform seeding of only $40\,\%$ or $15\,\%$ of the globe, to avoid ineffective regions like the tropics, has a cooling potential similar to their uniform cases due to a lack of cirrus SW radiative effect at higher latitudes in winter and a reduced natural background aerosol loading. Seeding a smaller area around $15\,\%$ of the globe in winter resulted in a similar ΔCRE response of
120 $-2.1\,\mathrm{Wm^{-2}}$, through mostly LW cloud forcing reduction while avoiding large compensating SW forcing increases (Storelvmo et al., 2014). Similarly, Gruber et al. (2019) simulated CCT using the higher-resolution ICON-ART model in a small Arctic region centered over Greenland. They also found large negative TOA LW anomalies from seeding, but only in their simulations where background mineral dust concentrations were limited. The CCT cooling potential decreased in their simulations with increasing background mineral dust concentrations.
125 Penner et al. (2015) re-evaluated the results by Storelvmo et al. (2013), Storelvmo and Herger (2014), and Storelvmo et al. (2014) using an updated version of CAM5 that not only included the cirrus ice nucleation competition between homogeneous

and heterogeneous nucleation, but also accounted for the consumption of water vapor by pre-existing ice transported into the cirrus regime. Additional updates were made to the dynamical environment to allow higher updraft velocities for the cirrus ice nucleation scheme, and to the aerosol environment to include secondary organic aerosols (SOAs) as potential INPs. Only their

130 seeding simulation with no pre-existing ice, no SOAs acting as INPs, and a limited updraft velocity showed any significant net negative TOA forcing up to $-0.74\,\mathrm{Wm^{-2}}$ in a similar optimal seeding particle concentration range as Storelvmo et al. (2013). All other simulations that included higher concentrations of INPs and higher updraft velocities resulted in positive net forcings. Gasparini and Lohmann (2016) extended these results using the ECHAM-HAM GCM with a cirrus ice nucleation scheme that also considered the competition between homogeneous and heterogeneous nucleation, and water vapor consumption on pre-

135 existing ice (Kärcher et al., 2006; Kuebbeler et al., 2014). Like Storelvmo et al. (2013), Storelvmo and Herger (2014), and Penner et al. (2015), Gasparini and Lohmann (2016) reported an optimal seeding particle concentration that was an order of magnitude lower than previous studies at $1\,\mathrm{L^{-1}}$. The maximum net TOA negative forcing in their full nucleation competition setup with the optimal seeding particle concentration was $-0.25\,\mathrm{Wm^{-2}}$, which was also smaller than in previous studies. Seeding with more than $1\,\mathrm{L^{-1}}$ resulted in warming from overseeding, which could be limited by the presence of pre-existing

140 ice particles. However, in all of their simulations the net TOA responses contained high uncertainty.

Overall, the more positive forcing responses presented by Gasparini and Lohmann (2016) were attributed to a decrease in the average size of ice crystals (ICs) post-seeding, and an increase in cirrus coverage in previously clear-sky areas, a potential side effect of seeding presented by Mitchell and Finnegan (2009). The efficiency of the seeding particles to consume water vapor was cited as the cause of the observed IC response, and as they highlight points to the dominance of heterogeneous nucleation to

145 cirrus formation in ECHAM-HAM. A source attribution analysis revealed that most cirrus formed via heterogeneous nucleation at a typical altitude of $200\,\mathrm{hPa}$, even in high latitude regions (Gasparini and Lohmann, 2016), contrasting previous studies by Storelvmo et al. (2013), Storelvmo and Herger (2014), and Penner et al. (2015). This difference between the nucleation mode dominance in different model setups is further evaluated in Gasparini et al. (2020), where even without seeding the global mean cirrus CRE is $2.0\,\mathrm{Wm^{-2}}$ greater in CAM5 than in ECHAM. With more heterogeneous nucleation present in cirrus in ECHAM-

150 HAM, it is less sensitive to seeding and has a much lower optimal seeding particle concentration than CAM5 (Gasparini et al., 2020). Overseeding can therefore occur more readily as water vapor consumption affects more particles.

Unintended side effects are likely with any climate intervention strategy. For example, a widely studied solar radiation management strategy, stratospheric aerosol injection, aims to increase planetary albedo by mimicking natural sulphur aerosol perturbations from volcanoes (Robock, 2000; Crutzen, 2006). However, numerous studies found that injecting such particles

155 into the stratosphere may deplete ozone and reduce the efficacy of renewable energy production (Crutzen, 2006; Robock et al., 2008; Murphy, 2009; Vaughan and Lenton, 2011). Alternatives to sulphur particles, like calcite, were investigated and found to lead to increased stratospheric ozone (Dykema et al., 2016; Keith et al., 2016), though using such particles may also impact cirrus clouds (Cziczo et al., 2019). In summary, assessing the potential side effects of any climate intervention strategy is crucial in order to understand future implementation.

160 To date, assessing the climate impact of CCT is limited to global or regional modeling studies that require a comprehensive understanding of the complex ice processes occurring in cirrus. With different approaches employed in each model, the

climate impact of CCT, including any unintended side effects, remains uncertain, which highlights the need for a consistent, physically-based approach to simulating the complex microphyiscal processes governing ice formation and growth in cirrus clouds (Gasparini et al., 2020). In this study, we investigate the climate impact of CCT using a new ice microphysics scheme in the ECHAM-HAM GCM that includes a prognostic treatment of ice sedimentation by introducing a single ice category, and an updated approach for calculating ice cloud fractions that allows for fractional cirrus gridbox coverage (Section 2). We perform CCT simulations using a cirrus ice nucleation scheme that accounts for the competition between homogeneous and heterogeneous nucleation, and depositional growth onto pre-existing ice particles (Section 2). Additional ice source number and mass mixing ratio tracers are implemented to directly investigate the impacts of seeding on the competition between the different ice nucleation modes. Results are presented in Section 3, followed by a discussion of our findings in Section 4. We present our conclusions in Section 5.

2 Methods

2.1 Model Description

We conduct our seeding experiments using the ECHAM6.3-HAM2.3 aerosol-climate GCM (Stier et al., 2005; Zhang et al., 2012; Stevens et al., 2013; Neubauer et al., 2019; Tegen et al., 2019). We use the horizontal resolution T63 ($1.875\degree$ x $1.875\degree$), with 47 vertical levels (L47) up to $0.01\,\mathrm{hPa}$, which corresponds to a vertical resolution of around 1 km in the upper troposphere at cirrus altitudes. The model timestep is 7.5 minutes.

The two-moment ice microphysics scheme by Lohmann et al. (2007), used in the default version of ECHAM6.3-HAM2.3, was succeeded by the Predicted bulk Particle Properties (P3) scheme by Morrison and Milbrandt (2015) that was ported to ECHAM-HAM by Dietlicher et al. (2018, 2019). It replaces an earlier method of artificially separating ice particles into different size classes (Levkov et al., 1992), rendering the use of the tuning parameter for the rate of snow formation unnecessary (Dietlicher et al., 2019). Instead, ice is represented with a single prognostic category based on mass-to-size relationships. With the single ice category no longer differentiating between in-cloud and precipitating ice, vertical advection and precipitation processes were also updated to include a substepping approach for prognostically solving ice sedimentation. This allows for sedimenting ice to be subjected to cloud processes as it falls, and for numerical stability within the cloud scheme (Dietlicher et al., 2018). For more specific information on P3 and its implementation within ECHAM6, please refer to Dietlicher et al. (2018, 2019).

A separate cirrus nucleation scheme by Kärcher et al. (2006) that was adapted for the ECHAM-HAM GCM by Kuebbeler et al. (2014) handles in-situ ice nucleation within cirrus clouds. It simulates the competition for water vapor between heterogeneous and homogeneous nucleation, and between depositional growth onto pre-exisitng ice particles that are transported into the cirrus regime from deep convective detrainment or from stratiform mixed-phase clouds. The scheme is based on the temporal evolution of ice saturation through the balance between the adiabatic cooling of rising air, with the associated saturation increase, and the diffusional growth of ice particles that consume the available water vapor. The adiabatic cooling rate is determined by the vertical velocity, which is represented by a grid-mean value plus a turbulent component based on the turbulent

195   kinetic energy (TKE), (Kuebbeler et al., 2014). Orographic effects on vertical velocity as well as small-scale gravity waves (Kärcher et al., 2006; Joos et al., 2010; Jensen et al., 2016a) in the upper troposphere are not included in this study. As the magnitude of the saturation ratio in the updraft is related to the vertical velocity, a fictitious downdraft is introduced to quantify the saturation ratio decrease by water vapor consumption onto ice (Kuebbeler et al., 2014). Muench and Lohmann (2020) updated the water vapor consumption by ice, following the diffusional growth equation (Lohmann et al., 2016). The temporal

200   change of the saturation ratio follows such that if the updraft is stronger than the water vapor consumption by pre-exisiting ice and heterogeneous INPs, then it may reach a suitable magnitude for homogeneous nucleation to occur. The opposite is true in weaker updraft regimes or in high INP concentration environments (Kärcher et al., 2006). A sub-time-stepping approach is employed in the cirrus scheme to simulate the rise of the air parcel and the subsequent saturation ratio decrease by ice formation, whereby the entire temporal evolution of the saturation ratio is simulated within a single model timestep.

205   To simulate the competition between homogeneous and heterogeneous nucleation, several freezing modes are introduced into the cirrus scheme, including pre-existing ice. In general, the cirrus nucleation scheme follows an "energy-barrier" approach, with pre-existing ice and the most efficient INP, dust (in the default setup), consuming water vapor at a lower ice saturation ratio (S_i). An ice formation event in each mode can occur as either a threshold freezing process or as a continuous freezing process (Muench and Lohmann, 2020). The former is based on the original cirrus scheme by Kärcher et al. (2006), whereby

210   ice forms by a particular mode when its critical ice saturation ratio ($S_{i,crit}$) is reached. In our setup, homogeneous nucleation of liquid-sulphate aerosols with a temperature-dependent $S_{i,crit}$ between 1.4 and roughly 1.75 (Koop et al., 2000), and immersion freezing of soluble material coated dust with a $S_{i,crit}$ of 1.3, act as threshold freezing modes. As a threshold process, all aerosol particles associated with the mode form ice that proceeds to deplete available water vapor and S_i. For dust immersion freezing, only 5% of the total dust aerosol concentration from the aerosol module, HAM, act as INPs within the mode, following

215   Gasparini and Lohmann (2016). Muench and Lohmann (2020) introduced the latter, continuous freezing process to account for the saturation-dependent activated fraction (AF) of INPs available for heterogeneous nucleation. We include deposition on insoluble accumulation and coarse size mode (Stier et al., 2005; Zhang et al., 2012; Tegen et al., 2019) dust particles as continuous freezing modes. The AF is calculated using a temperature-dependent $S_{i,crit}$ threshold of 1.2 for T > 220 K, and 1.1 for T $\leq$ 220 K based on laboratory measurements by Möhler et al. (2006). At every timestep in the cirrus scheme, the AF of

220   these modes is calculated, and if ice forms it is added to the ice concentration.

     In this study, we introduce two significant improvements to the representation of the continuous freezing modes. Firstly, we implement a budgeting approach for the available dust INPs that was not previously included in the latest version of the cirrus scheme. This reduces the potential to over-predict the amount of ice that forms heterogeneously through deposition onto dust particles. Secondly, we introduce the differential AF approach by Kärcher and Marcolli (2021) that further addresses the

225   over-prediction issue associated with heterogeneous nucleation on dust INPs when using an INP-budgeting approach. In this new approach we no longer use the cumulative AF of the current cirrus-model time-step based on the current S_i. Instead, only if the cumulative AF of the current cirrus-model time-step is greater than the previous step is the differential AF calculated as the difference between the cumulative AF of the current cirrus-model time-step and the previous cirrus-model time-step cumulative AF. As a short conceptual example, if in the first cirrus-model time-step the cumulative AF $= 5\%$ and in the second

230   cirrus-model time-step the cumulative AF = $10\,\%$, the differential AF for the second cirrus-model time-step would be $5\,\%$. This has the potential to drastically reduce the amount of heterogeneous nucleation on dust particles, and may have wider implications on CCT efficacy, not considered in previous studies (Gasparini and Lohmann, 2016; Gasparini et al., 2017, 2020).

Following Gasparini and Lohmann (2016), we introduce seeding particles as a separate threshold freezing mode into the cirrus scheme for temperatures below $238\,K$, increasing the competition for available water vapor. All seeding particles can

235   nucleate ice with a $S_{i,crit}$ (hereafter seeding particle critical saturation ratio ($S_{i,seed}$)) of 1.05 (Storelvmo and Herger, 2014), and later with $S_{i,seed}$ = 1.35 (below). The seeding particles have a modal radius of $0.5\,\mu m$ like in Gasparini and Lohmann (2016). We perform uniform global seeding with no spatial or temporal variability in seeding particle concentration for comparability with previous GCM studies, except for an altitude restriction below $100\,hPa$ to minimize seeding of the stratosphere. This seeding restriction to altitude levels below $100\,hPa$ (i.e. higher pressure levels) is in line with proposed real-world delivery

240   mechanisms for seeding particles with commercial aircraft (Mitchell and Finnegan, 2009).

Cloud cover is based on the diagnostic approach by Sundqvist et al. (1989), (S89) that assumes fractional cloud formation exists due to relative humidity (RH) variability within the gridbox. The formulation was developed for liquid (warm) clouds, using a critical RH (RH_{crit}) above which fractional cloud cover in a gridbox can occur. Full grid-box coverage occurs when grid-mean RH reaches $100\,\%$ with respect to liquid water. This formulation works well for warm clouds, but as Kuebbeler

245   et al. (2014) and Dietlicher et al. (2018, 2019) note, it breaks down for mixed-phase clouds (T < 273 K) that may or may not include ice, presenting a difficult choice between RH with respect to liquid (RH_l) or ice (RH_i) for full gridbox coverage. The S89 approach for pure ice clouds (T < 235 K) is analogous to warm clouds in earlier versions of our model, where instead of liquid water saturation, full coverage occurs at ice saturation. As Kuebbeler et al. (2014) explain, when accounting for the ice supersaturation required for homogeneous or heterogeneous nucleation, this leads to full gridbox coverage of freshly nucleated

250   cirrus clouds, an inconsistency between cloud fraction and the microphysics scheme (Kärcher and Burkhardt, 2008). This also may explain the high cirrus CRE in ECHAM6 found by Gasparini and Lohmann (2016). Dietlicher et al. (2019) updated the cloud fraction formulation for pure ice clouds to differ from liquid clouds by updating the RH bounds in which an ice cloud can form. In our version of the model for this study, fractional ice cloud coverage no longer exists below ice saturation (i.e. RH_{crit} = $100\,\%$ RH_i, S_i = 1.0), with full coverage following the Koop et al. (2000) theory for homogeneous nucleation of solution

255   droplets. The difference between the two schemes is illustrated in Figure 1 that was adapted from Dietlicher et al. (2019). Both approaches use saturation adjustment to calculate ice cloud fractions, but D19 increases the bounds for ice cloud formation to allow for ice supersaturation, which is more realistic than the S89 approach that does not allow for ice supersaturation. For example with Figure 1, if ice were to form at $218\,K$ in an environment with S_i = 1.6, then D19 would adjust the supersaturation to that for aqueous solution droplets following Koop et al. (2000) to form a cirrus cloud that would fully cover the gridbox.

260   S89 works in the same way, but instead would adjust the supersaturation to ice saturation (S_i = 1.0) and also would produce a fully covered gridbox.

Additional ice number and mass mixing ratio tracers were added to the model, following Dietlicher et al. (2019), to trace the origin of in-situ cirrus ice directly. We include two tracers for ice from homogeneous and heterogeneous nucleation, with additional tracers for heterogeneously-formed ice on dust and seeding particles, the sum of which equates to the total in-
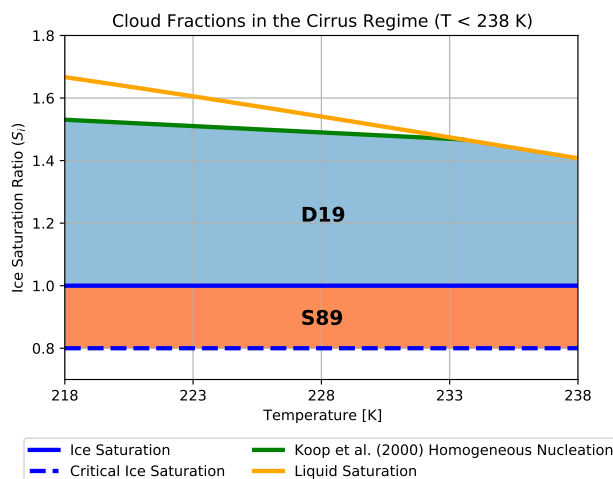
Figure 1. Cloud fraction schematic adapted from Dietlicher et al. (2019) showing the difference between the D19 and S89 approaches for calculating ice cloud fractions. The shaded areas show the temperature versus ice saturation ratio conditions where clouds can form, with the orange area for S89 and the blue area for D19. The blue line is the ice saturation line ($S_i = 1.0$), the blue dotted line is the critical ice saturation line for cloud formation in the S89 approach, the orange line is for liquid saturation with respect to ice saturation, and the green line is the homogeneous nucleation limit according to Koop et al. (2000).

situ heterogeneously-nucleated ice tracer. The implementation of these tracers highlighted erroneous scaling of the aerosol concentrations of the various freezing modes in the cirrus ice nucleation competition scheme by the total amount of pre-existing ice. This was updated to properly account the fraction of each mode of the pre-existing ice, excluding the dust deposition modes, which were updated with INP and the new differential AF (Kärcher and Marcolli, 2021) as detailed above. These updates warranted a re-tuning of the model to target the balance between global annual mean, TOA SW and LW fluxes (Lohmann and Ferrachat, 2010; Mauritsen et al., 2012; Neubauer et al., 2019). Ice self-collection (ccnislf) was doubled to 6.0 from its original value in the base version of the model (Dietlicher et al., 2019) to account for a too weak TOA SW and LW fluxes. This adjustment strengthened both TOA fluxes, but the LW flux was still too weak. Therefore, to compensate the auto-conversion rate from cloud liquid water to rain within convective cores was increased to 1.77. As convective clouds also impact TOA SW fluxes, we adjusted the auto-conversion rate within stratiform liquid clouds (γ_r) to 2.4. All other tuning parameters were kept the same as the "HET_CIR" configuration in Dietlicher et al. (2019). We also note a too negative net CRE after tuning, which Dietlicher et al. (2019) attributed to a structural issue within the model. In addition, our five-year global mean LW CRE is $21.8\,\mathrm{W m^{-2}}$, which is weaker by about $0.2\,\mathrm{W m^{-2}}$ than the lower range of the observations (Neubauer et al., 2019).

2.2 Experimental Setup

We performed cirrus seeding simulations using P3 with the cirrus scheme coupled to the new fractional ice cloud cover formulation (D19) described above. We examined seeding with full nucleation competition between heterogeneous, homogeneous, and

Table 1. Experimental setup for cirrus seeding for the two ice-cloud fraction schemes. Both configurations include seeding particle concentrations of 0.1, 1, 10, and 100 L^{-1}. In addition, seeding is conducted for a seeding particle critical ice saturation ratio (S_i) of 1.05 and 1.35. The "Full" in the reference simualtions refers to full ice nucleation competition between pre-existing ice, heterogeneous nucleation on minereal dust particles, and homogeneous nucleation of liquid sulfate aerosols in the in-situ cirrus scheme (Kärcher et al., 2006; Kuebbeler et al., 2014).

Ice-cloud fraction scheme	Description	Reference Simulation	$S_{i,seed}$ = 1.05	$S_{i,seed}$ = 1.35
D19	new cloud fraction by Dietlicher et al. (2018, 2019)	Full_D19	Seed0.1	Seed0.1_1.35
			Seed1	Seed1_1.35
S89	original cloud fraction by Sundqvist et al. (1989)	Full_S89	Seed10	Seed10_1.35
			Seed100	Seed100_1.35

pre-existing ice. Additionally, we tested the original S89 ECHAM6 ice cloud cover approach (Stevens et al., 2013; Neubauer et al., 2014, 2019) within the framework of the P3 scheme (S89); we did not re-tune the model for simulations using S89 in order to examine the sensitivity of cirrus seeding to the ice cloud fraction scheme. Previous CCT studies include additional simulations in which they allow only homogeneous nucleation to occur in cirrus. Here, we chose to pursue full nucleation competition as a more realistic approach to examine the impact of seeding particles, mimicking a real-world implementation. For both model configurations (see Table 1) we implemented seeding INPs at every timestep as an additional freezing mode in the cirrus nucleation scheme such that only gridboxes that are saturated with respect to ice (i.e. S_i = 1.0) are seeded. We test four seeding INP concentrations of 0.1, 1, 10, and 100 INP L^{-1} to represent the spread of concentrations tested in previous studies (Storelvmo and Herger, 2014; Penner et al., 2015; Gasparini and Lohmann, 2016). Each simulation was run for five years between 2008 and 2012, inclusive, with three months of spin-up from 1st October 2007. Monthly mean sea surface temperatures and sea ice coverage are prescribed, and emissions are from the year 2010 following CMIP6 methodology (van Marle et al., 2017; Hoesly et al., 2018).

The $S_{i,seed}$ of 1.05 follows Storelvmo and Herger (2014) and Gasparini and Lohmann (2016), and is based on suggestions of a potential seeding particle material, bismuth tri-iodide (BiI_3) (Mitchell and Finnegan, 2009). It is unclear whether this $S_{i,seed}$ can be applied to a realistic seeding particle material. Therefore, to test the sensitivity of ice nucleation competition to the seeding INP, we run additional seeding simulations with all seeding particle concentrations described above, with a $S_{i,seed}$ of 1.35 (Table 1). This ensures that seeding can occur in ice supersaturated environments below the lower homogeneous nucleation $S_{i,crit}$ threshold around 1.40 and above the maximum $S_{i,crit}$ for dust of 1.3.

2.3 Uncertainty

We take particular care to quantify significance in our results, following the "false discovery rate (FDR)" method by Wilks (2016). The updated approach for conducting independent t-tests accounts for high spatial correlation of neighboring grid-

points, i.e. the null hypothesis cannot not be as widely rejected when calculating significance. We calculate significance based on the inter-annual variability over the five years of simulation (Section 2.2). The inter-annual variability is also used to calculate the 95 % confidence interval around the five-year mean.

305 ## 3 Results

3.1 Model Validation

We start by evaluating the model with the new P3 ice microphysics scheme and the new D19 ice-cloud fraction approach for the unseeded reference case, by comparing ICNC data to the latest compilation of in-situ aircraft measurements by Krämer et al. (2016, 2020) in Figure 2. Model results represent the five-year mean temperature versus ICNC between 2008 and 2012.

310 The observational data comprise multiple in-situ aircraft field campaigns between 1999 and 2017, totalling around 90 hours of flight data (Krämer et al., 2020), with different meteorological situations captured in the tropics, mid-latitudes, and the Arctic; southern high latitudes are not included. Although this is a much more significant compilation of observational data than was previously available, there remains a caveat that these data are not representative of the entire atmosphere (Krämer et al., 2020).

Model data are presented in Figure 2a and the observations in Figure 2b. The median ICNC per temperature bin between

315 $180\,\mathrm{K}$ and $250\,\mathrm{K}$ is also plotted for both data sets, with the observational median also plotted with the model data for comparison. Model-median ICNC values agree rather well with the observational median at temperatures between roughly $190\,\mathrm{K}$ and $230\,\mathrm{K}$, and above $240\,\mathrm{K}$. Between $230\,\mathrm{K}$ and $240\,\mathrm{K}$ the model-median diverges above the observational median where it does not capture the more frequent occurrence of lower ICNC values. Both the model and observations capture the tailing-off of ICNC at temperatures warmer than $240\,\mathrm{K}$, with the model slightly lower than the observations. These phenomena may be

320 linked to the default parameterization for heterogeneous nucleation on mineral dust particles in mixed-phase clouds in ECHAM by Lohmann and Diehl. (2006), which is based on dust immersion freezing rates. Villanueva et al. (2021) conducted several sensitivity tests with ECHAM-HAM using this default freezing-rate-based scheme and an newer AF approach based on dust particle surface area and active site density. They found better agreement with satellite-based observations using the AF approach as compared to the default rate-based approach, and noted an under-prediction of mixed-phase ice with the latter that led

325 to a higher abundance of cloud droplets being transported into the cirrus regime where they could undergo homogeneous nucleation. Our model median ICNC values between $230\,\mathrm{K}$ and $250\,\mathrm{K}$ indicate a similar behavior. The higher ICNC values between $230\,\mathrm{K}$ and $240\,\mathrm{K}$, as compared to the observations, are likely of liquid-origin. Whereas, the lower ICNC values above $240\,\mathrm{K}$ are likely due to the under-prediction of mixed-phase ice using the default rate-based scheme for dust immersion freezing. The Villanueva et al. (2021) study suggests using a different approach for mixed-phase cloud glaciation for better comparability

330 to observations and to address this issue of an over-abundance of liquid-origin cirrus ice. Krämer et al. (2020) suggest that these liquid-origin cirrus in the mid-latitudes originate from warm conveyor belts or mesoscale convective systems. Therefore, their formation is tied to a stronger dynamical forcing that allows for abundant homogeneous nucleation from numerous cloud droplets being transported into the cirrus regime. As CCT targets in-situ formed cirrus in regions with less dynamical forcing, we deem this over-prediction of ICNC values insignificant relative to our study (Gasparini et al., 2017).
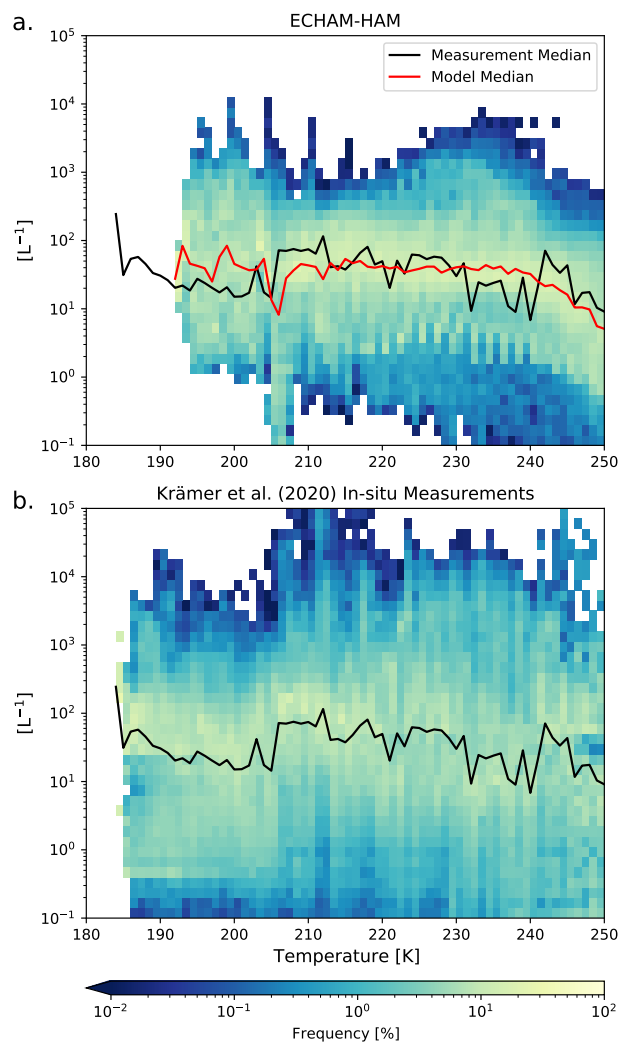
Figure 2. ICNC frequency diagrams for ice crystals with a diameter of at least 3 µm as a function of temperature between 180 K and 250 K binned like in Krämer et al. (2020) for every 1 K. The five-year global mean data from the model is plotted in (a) and the compilation of in-situ flight data from Krämer et al. (2020) is plotted in (b). The red line in the upper plot represents the binned median ICNC value of the model data, and the black line in both plots is the same value for the observational data.

The model does not capture the ICNC occurrence at temperatures below roughy 195 K. According to Krämer et al. (2020) ICNC values at such cold temperatures originate from tropical deep convection. A simple analysis on the number of data points belonging to this temperature regime shows that in the observations (not shown), there is a large drop-off in the number of recorded points. Therefore, these measurements make up a small portion of the total observational dataset. Furthermore, CCT in a real-world context would target in-situ formed cirrus away from systems with strong dynamical forcing (Gasparini

Table 2. Five-year annual global mean net top-of-atmosphere total radiative balance (TOA) and net CRE in $\mathrm{Wm^{-2}}$ for D19 and S89 ice-cloud cloud fraction approaches for seeding with $S_{i,seed}$ = 1.05. Each quantity includes the $95\,\%$ confidence interval equating to two standard deviations of the mean values of the five-year data.

Seeding Concentration [$\mathrm{L^{-1}}$]	0.1	1	10	100
D19 net TOA	-0.17 ± 0.32	-0.36 ± 0.19	0.30 ± 0.19	4.27 ± 0.40
S89 net TOA	-0.24 ± 0.47	0.17 ± 0.47	2.18 ± 0.45	8.95 ± 0.36
D19 net CRE	$7.51\mathrm{e}{-4} \pm 0.29$	-0.13 ± 0.26	0.81 ± 0.27	3.85 ± 0.36
S89 net CRE	0.13 ± 0.40	0.50 ± 0.41	2.66 ± 0.43	8.01 ± 0.30

340 et al., 2017), like in the tropics. Overall, for the purposes of our CCT analysis we find that the model agrees remarkably well with the Krämer et al. (2020) measurements for in-situ formed cirrus.

3.2 D19 versus S89 seeding

The net global-mean radiative balance between TOA SW and TOA LW fluxes, including the net CRE is presented in Figure 3a and c, respectively, for $S_{i,seed}$ = 1.05. The results are tabulated in Table 2 along with the $95\,\%$ confidence interval. Small

345 negative radiative anomalies are evident for both D19 and S89 for Seed0.1 (Table 1), but contain high uncertainty. We find the maximum amount of cooling for D19 of nearly $-0.4\,\mathrm{Wm^{-2}}$ for Seed1 (Table 2). S89 may also produce some cooling for Seed1 due to the wide uncertainty surrounding the mean value. For a seeding concentration of 10 INP $\mathrm{L^{-1}}$ and larger the radiative anomalies indicate an overseeding response as no cooling is evident. Furthermore, the differences between the two cloud cover approaches become abundantly clear. The largest warming occurs for Seed100, with $4.3\,\mathrm{Wm^{-2}}$ (D19) and

350 $9.0\,\mathrm{Wm^{-2}}$ (S89). These responses are an order of magnitude larger than the maximum TOA anomaly found by Gasparini and Lohmann (2016) of $0.5\,\mathrm{Wm^{-2}}$ at the same seeding particle concentration and for a similar configuration of the cirrus scheme. Instead, our results more closely resemble their simulations where seeding was applied to cirrus that could form only by homogeneous nucleation, but are more than two times what they found at a seeding concentration of 100 INP $\mathrm{L^{-1}}$. This difference in results further highlights the importance of a consistent approach to simulate cirrus ice microphyiscs (Gasparini

355 et al., 2020), and will be discussed further in Section 4. In addition, the maximum responses shown here are well above the latest available IPCC estimate at the time of writing of the radiative forcing from a doubling of atmospheric CO_2 from the pre-industrial period of $3.7\,\mathrm{Wm^{-2}}$ (Flato et al., 2013; Myhre et al., 2017), highlighting the potential dangerous side-effects of cirrus seeding.
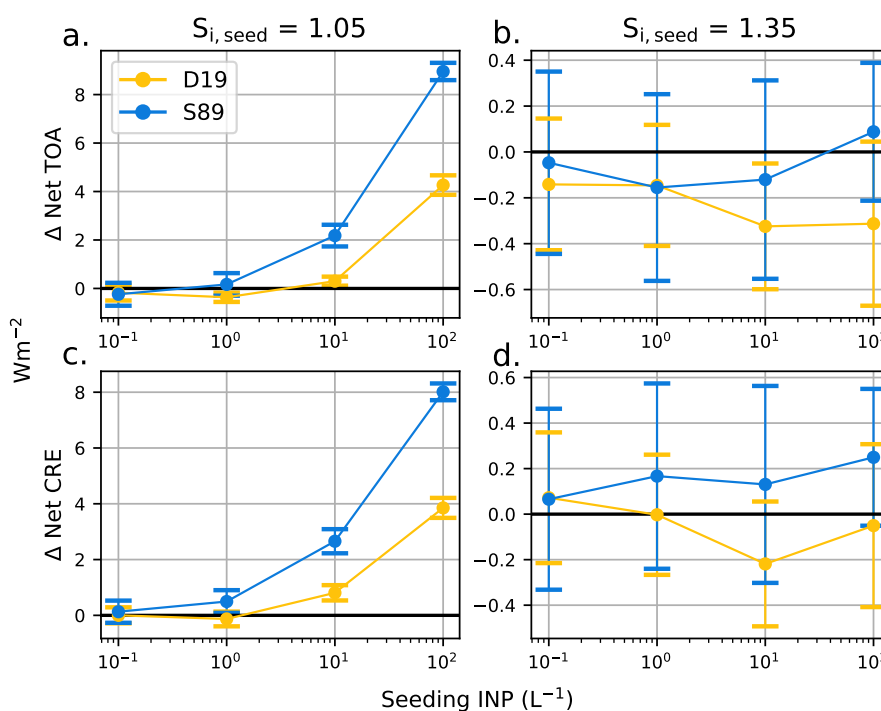
Figure 3. Five-year mean global mean net top-of-atmosphere (TOA) radiative balance anomalies in $\mathrm{Wm^{-2}}$ between total SW and longwave fluxes, and cloud radiative fluxes comprising the CRE. Anomalies are defined as the differences between each seeding simulation and the reference simulation without seeding. The left column (a,c) shows the radiative anomalies for simulations with $S_{i,seed}$ = 1.05, and the right column (b,d) is the same for $S_{i,seed}$ = 1.35. The errors bars represent the 95 % confidence (2σ). Note the differences in scales for the $S_{i,seed}$ = 1.05 plots and the $S_{i,seed}$ = 1.35 plots.
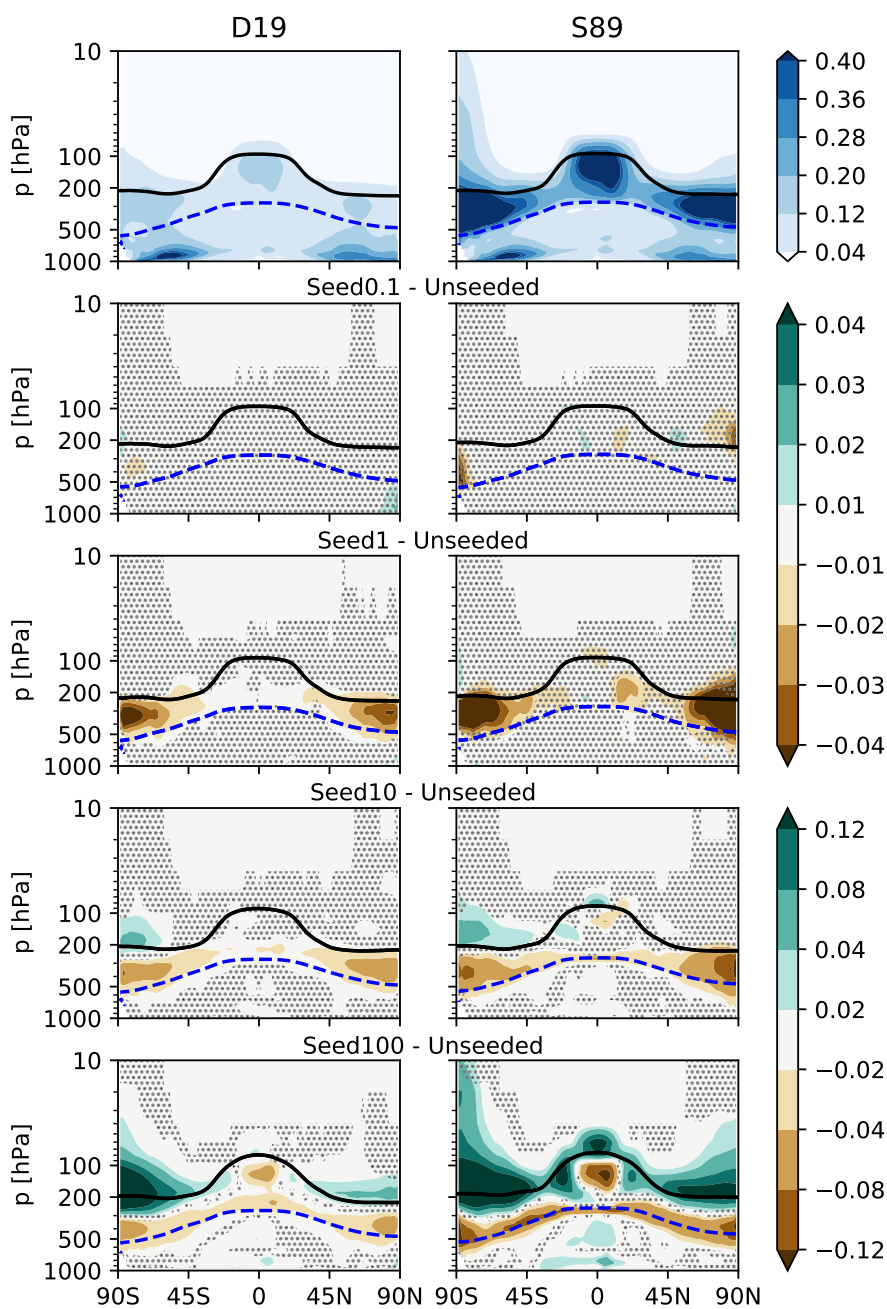
Figure 4. Five-year zonal mean cloud fractions [0-1] on pressure levels [hPa] for D19 and S89 ice-cloud fraction approaches for the unseeded reference cases (top-panels). The cloud fraction differences to the respective unseeded reference case are plotted in the subsequent rows for $S_{i,seed}$ = 1.05: Seed0.1 (second row), Seed1 (third row), Seed10 (fourth row), and Seed100 (fifth row). The black line is the five-year mean zonal mean WMO-defined tropopause height on pressure levels, and the blue dashed line is the 238 K isotherm. The stippling in the difference plots shows insignificant data points on the 95 % confidence level according to the independent t-test controlled by the "false discovery rate" method.

Cloud effects are the largest contributor to the TOA radiative anomalies (Figure 3c and Table 2), and even, in the case of Seed10, are greater than the total net TOA anomaly, likely due to rapid adjustments in response to seeding, like cloud fraction changes. In the Seed100 case, the net CRE anomalies make up roughly $90\,\%$ of the total TOA for both D19 and S89. To examine this further, in particular the overseeding at high seeding particle concentrations, we show the zonal mean cloud fraction anomalies between each seeding simulation and their respective reference simulation for both cloud fraction schemes in Figure 4. Firstly, the difference between D19 and S89 stands out from the respective reference simulations (top panels). With the larger S_i bounds for ice cloud fractions in D19, there is a clear cloud fraction reduction within the cirrus regime, above the blue dotted line in Figure 4, which leads to less warming in the reference simulation compared to S89. The new cloud fractions in D19 were found to agree better with the observed satellite product from CALIPSO than the original S89 approach (Dietlicher et al., 2019), with higher correlation and lower root mean square error. Secondly, a significant pattern in the zonal cloud fraction does not emerge for Seed0.1. Seeding with Seed1 appears to produce the desired reduction in cirrus cloud fractions by more than $4\,\%$ that would lead to cooling. A different pattern emerges for Seed10 and Seed100, where what appears as a shift in cloud height starts developing within the cirrus regime at these seeding concentrations and reaches a maximum for Seed100. Seeding decreases cloud fraction by up to $8\,\%$ and $12\,\%$ in D19 and S89 respectively in the mid-troposphere between $300\,\mathrm{hPa}$ and $800\,\mathrm{hPa}$ at higher latitudes, and between $300\,\mathrm{hPa}$ and $100\,\mathrm{hPa}$ in the tropics. Note that the tropopause is located at roughly $200\,\mathrm{hPa}$ in polar regions and at $100\,\mathrm{hPa}$ in the tropics, as shown by the black line in Figure 4. Cloud fraction increases by more than $12\,\%$ over wider areas in the upper troposphere over the poles and over all latitudes in the lower stratosphere. Here the difference between the two cloud fraction approaches is also clear, with S89 showing much more extensive regions of cirrus cloud fraction increases in the stratosphere than D19. The difference between the cloud fraction approaches is discussed further in Section 4. In the troposphere overseeding leads to a reduction of lower lying cirrus and the increase in higher and colder cirrus, which in turn lead to the radiative anomalies discussed above. Meanwhile, the overseeding response is amplified by the unrealistic increases of cloud fraction in the stratosphere.

Next, we examine the microphysical response to seeding in Figure 5, which shows the ICNC anomalies for Seed1 (a-b) and Seed100 (c-d) for both D19 and S89. With the negative TOA anomalies and the decrease in cloud fractions for Seed1, we expected seeding to have the desired impact of decreasing ICNC in the troposphere through sedimentation of fewer larger ice crystals. This effect is not evident here. Instead, determining an exact ICNC response for Seed1 is rather difficult due to ICNC anomaly heterogeneity. For example, for D19 Seed1 (Figure 5a), in some areas we find that seeding produces fewer ice particles at higher altitudes and more at lower altitudes. This is in line with one of the desired outcomes of CCT to produce ice at lower altitudes, i.e. warmer temperatures, which emits more LW than higher-altitude ice, thus inducing a cooling effect. However, in our case, the shift is from ice in the lower stratosphere to more ice within the cirrus regime in the troposphere. On top of this, our FDR analysis (Wilks, 2016) reveals that the Seed1 ICNC anomalies contain high uncertainty. Despite this, the cooling we find for Seed1 with D19 appears to originate from fewer clouds that on-average contain more ice, which strengthens the negative SW CRE by roughly $-0.4\,\mathrm{Wm^{-2}}$ and outweighs the positive LW CRE anomaly around $0.3\,\mathrm{Wm^{-2}}$. The TOA LW flux also increases only slightly due to fewer cirrus clouds, and contributes to the net cooling effect in Figure 3.
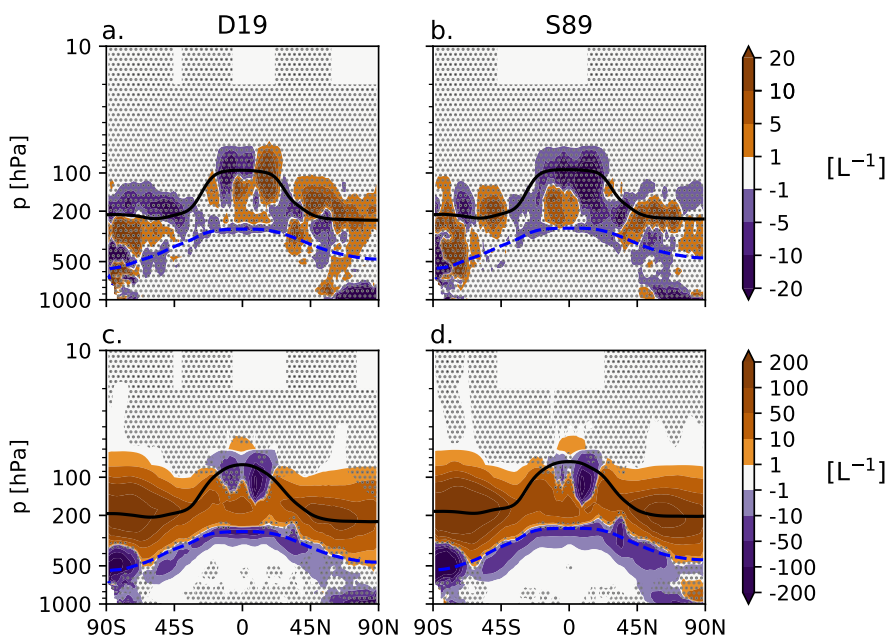
Figure 5. Five-year zonal mean ICNC $S_{i,seed}$ = 1.05 anomalies [L^{-1}] for both D19 and S89 ice-cloud fraction approaches. Seed1 anomalies are presented in a and b, and Seed100 anomalies are presented in c and d. The black line is the five-year mean zonal mean WMO-defined tropopause height on pressure levels, and the blue dashed line is the 238 K isotherm. The stippling in the difference plots shows insignificant data points on the 95 % confidence level according to the independent t-test controlled by the "false discovery rate" method.

The ICNC anomalies are much clearer for the extreme case, Seed100, than the Seed1 anomalies (Figure 5c-d), and will be examined further in this section. Positive ICNC anomalies exceeding 200 L^{-1} are shown at all latitudes throughout the
395 troposphere, and into the lower stratosphere at higher latitudes. Here the ICNC anomalies are in line with the cloud fraction anomalies in Figure 4. There is a loss of the lowermost ice crystals that also extends into the mixed-phase regime (below the blue dashed line in Figure 5), while the ICNC in the cirrus regime increases. This is most likely due to the proficiency of seeding particles to nucleate ice, leading to more numerous and smaller ice crystals compared to the unseeded case. In fact, we find that ice crystals (ICs) decrease in size on average by more than 4.0 μm in the cirrus regime for Seed100 (not shown). The
400 more abundant smaller ICs in the cirrus regime, therefore, enhance the cirrus LWCRE to produce the strong positive Seed100 net TOA anomaly in Figure 3.

It is clear that seeding particles in Seed10 and Seed100 lead to an overseeding effect, with wide impacts on the total ICNC. However, for a direct view of the impact seeding particles have on ice nucleation competition, Figure 6 shows the ice number tracer (Section 2.1) anomalies for Seed100. The tracers include in-situ cirrus ice numbers from homogeneous and heteroge-
405 neous nucleation, with additional tracers for heterogeneously formed ice on mineral dust particles and seeding particles. Firstly, the anomalies presented in Figure 6 are mainly constrained to the cirrus regime, the area above the blue-dashed line, and the

lower stratosphere, with some extension of anomalies into the lower-lying mixed-phase regime. In terms of ice nucleation competition, Seed100 shows the desired effect by decreasing homogeneously-nucleated ice by more than $200\,\mathrm{L^{-1}}$ in the middle to upper troposphere in both D19 and S89. The opposite effect occurs in the stratosphere where homogeneously-nucleated

410 ice increases. As there is a clear separation, this stratospheric effect is discussed further in Section 3.3. This reduction of homogeneous nucleation in the troposphere is outweighed by the wider-spread increases in heterogeneous nucleation globally throughout the middle to upper troposphere and into the lower stratosphere for both ice cloud fraction approaches, leading to the positive net TOA and CRE anomalies (Figure 3). For Seed100 the heterogeneous signal is clearly dominated by seeding particles that act to overtake natural processes, including heterogeneous nucleation on dust as well as homogeneous nucleation.

415 While this effect occurs in both D19 and S89, the spatial extent of the ICNC responses is more widespread in the latter in line with the smaller S_i bounds for calculating ice cloud fractions.

We also find seeding particles from the cirrus regime ending up in the mixed-phase regime (below the dashed line in Figure 6), pointing to potential impacts on lower-lying cloud layers from seeding. In fact, vertical profiles of IWC and liquid water content (LWC) for D19 only in Figure 7 confirm this behavior. The positive Seed100 IWC anomaly within the cirrus

420 regime right of the vertical black line in Figure 7 is in line with the total ICNC and ICNC tracer anomalies. We also find that ice increases to a smaller extent in the upper portion of the mixed phase regime, also in line with the tracer anomalies above. The main impact of seeding appears as a reduction of IWC in wider areas of the mixed-phase regime, which is likely due to amplified ice residence times in the cirrus regime fuelled by smaller ICs that weaken the sedimentation flux. With less ice falling into the mixed-phase regime at lower altitudes, LWC anomalies responded positively (Figure 7b) due to less efficient

425 riming and/or cloud droplet depletion via the Wegener–Bergeron–Findeisen (WBF) process. This results in a stronger SW CRE by about $3.7\,\mathrm{Wm^{-2}}$ for Seed100. However, this is outweighed by the larger LW CRE positive anomaly of $7.5\,\mathrm{Wm^{-2}}$ due to optically thicker in-situ cirrus (Krämer et al., 2020).

The patterns found in the TOA radiative anomalies, and the ICNC and IWC anomalies can be explained by the competition for water vapor during the formation of in-situ cirrus ice. The cirrus scheme is called during every time-step in the model, and

430 the nucleation of new ice crystals occurs only if cirrus conditions ($T < 238\,\mathrm{K}$) are met. Seeding particles efficiently form new ice crystals with a relatively low $S_{i,seed} = 1.05$. They consume water vapor with increasing efficiency at higher concentrations, leaving little supersaturated vapor left for other processes to occur, as indicated by the reduction of homogeneous nucleation and heterogeneous nucleation on mineral dust particles. This phenomenon goes beyond the traditional understanding of overseeding, where only homogeneous nucleation suppression was documented, coupled to a higher number of ICs nucleated

435 on seeding particles (Storelvmo et al., 2013). Rather, our results show that overseeding leads to an ice nucleation competition alteration with the suppression of heterogeneous nucleation on mineral dust particles on top of homogeneous nucleation suppression. In relation to the cloud fraction responses (Figure 4), overseeding in our model appears to lead to the desired reduction of mid-troposphere clouds. However, at higher altitudes seeding particles overtake natural processes to form higher cloud fractions. As these clouds are in general colder, increases in their coverage lead to a larger TOA warming described

440 above.
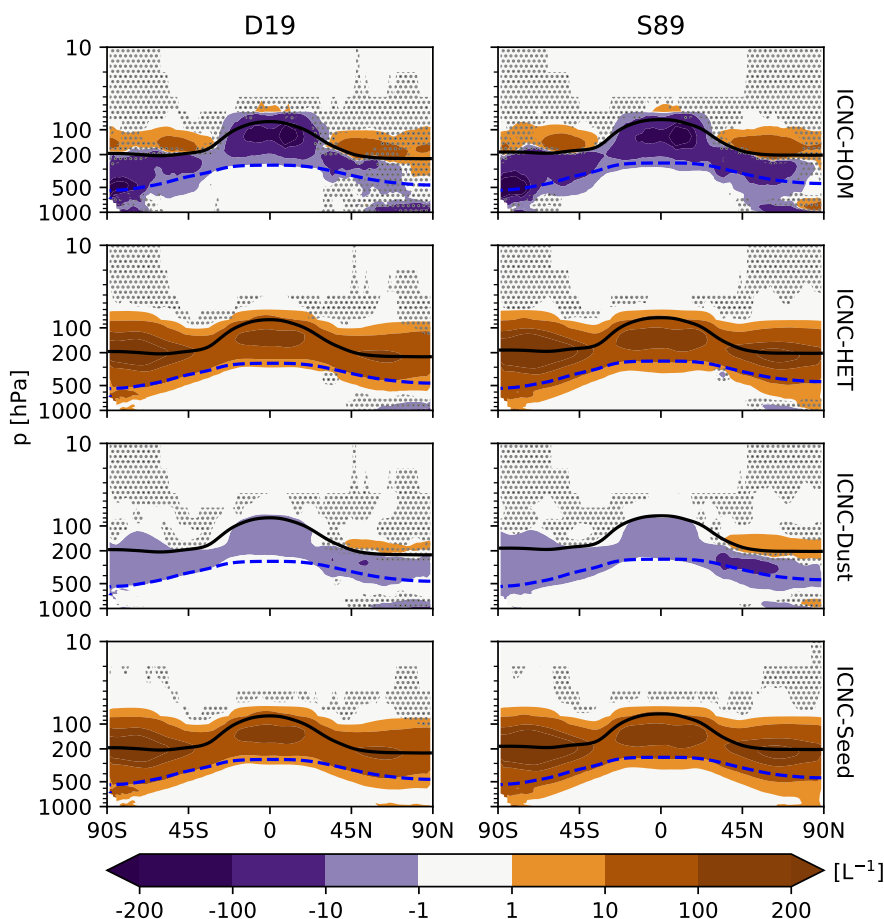
Figure 6. Five-year zonal mean in-situ ice number tracer [L^{-1}] anomalies between the simulation with 100 seeding INP L^{-1} for $S_{i,seed}$ = 1.05 and the respective unseeded reference case for both D19 and S89 ice-cloud fraction approaches. Each tracer is for in-situ cirrus ice only, and does not include ice formed in the mixed-phase regime. The top row is the difference for in-situ homogeneously-nucleated ice number, the second row is the difference for the in-situ heterogeneous number, the third row is the difference for the heterogeneously-nucleated ice number formed on mineral dust particles, and the last row is the difference for the heterogeneously-nucleated ice number formed on seeding particles. The black line is the five-year mean zonal mean WMO-defined tropopause height on pressure levels, and the blue dashed line is the 238 K temperature contour. The stippling in the difference plots shows insignificant data points on the 95 % confidence level according to the independent t-test controlled by the "false discovery rate" method.

Overseeding occurs with both D19 and S89 ice cloud fraction approaches, but is more widespread with the narrower S_i bounds used in the latter. With seeding particles present in every gridbox of the cirrus scheme and their relatively low $S_{i,seed}$, even small increases in INPs and hence the amount of ice in an ice-supersaturated environment can lead to dramatic cloud fraction increases with S89. In addition, the low $S_{i,seed}$ = 1.05 "out-competes" all other freezing modes to alter nucleation
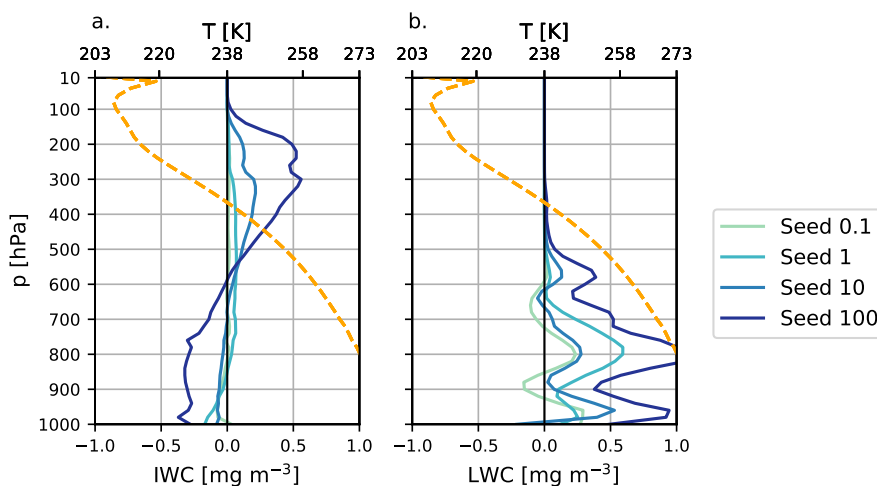
Figure 7. Five-year annual global mean (a) IWC and (b) LWC vertical anomaly profiles for D19 for all seeding particle concentrations for $S_{i,seed}$ = 1.05. The orange dotted line represents the five-year global mean temperature vertical profile centred around the homogeneous freezing temperature limit (238 K).

445   competition away from natural processes and towards seeding particles with both schemes. As this critical saturation ratio threshold is somewhat arbitrary, we next investigate the seeding sensitivity with INPs needing a higher $S_{i,seed}$ = 1.35 for nucleation.

3.3   1.05 S_i versus 1.35 S_i seeding

Additional sensitivity tests were conducted by increasing $S_{i,seed}$ to 1.35 (1.35-seeding) in an effort to limit the overseeding
450   found when seeding with $S_{i,seed}$ = 1.05 (1.05-seeding). Figure 3b presents the net TOA radiative anomaly for both cloud fraction approaches for 1.35-seeding; results are also presented along with the 95 % confidence interval in Table 3. Note the difference in scale to the 1.05-seeding TOA plot (Figure 3a). Not only does 1.35-seeding lead to a drastic reduction in magnitude in the net TOA anomalies for both D19 and S89, but also to a small cooling effect for all seeding concentrations, excluding the small positive TOA anomaly for S89 Seed100, meaning that the desired cooling from seeding in our model can occur over a
455   broader range compared to early CCT studies (Storelvmo et al., 2013). TOA anomalies are stronger in D19 than in S89, with the strongest negative anomaly of $-0.3\,\mathrm{Wm^{-2}}$ for Seed10. This is in part, due to a strengthening of the LW CRE with D19 (i.e. warming) that is outweighed by a stronger SW CRE (i.e. cooling). The smaller net TOA anomalies for S89 are driven by a weakening SW CRE with seeding that is partially compensated by a weakening LW CRE, except in the Seed100 case where the increase in LW CRE outweighs the stronger SW CRE. However, consistent across both cloud fraction approaches
460   is the large uncertainty relative to the absolute response, leading to uncertain responses in the net TOA radiation and CRE in Figure 3c,d. The only exception is for D19 Seed10, which on the 95 % confidence level shows a net cooling effect.

Table 3. Five-year annual global mean net top-of-atmosphere total radiative balance (TOA) and net CRE in $\mathrm{Wm^{-2}}$ for D19 and S89 ice-cloud fraction approaches for seeding with $S_{i,seed}$ = 1.35. Each quantity includes the 95 % confidence interval equating to two standard deviations of the mean values of the five-year data.

Seeding Concentration [$\mathrm{L^{-1}}$]	0.1	1	10	100
D19 net TOA	-0.14 ± 0.29	-0.15 ± 0.26	-0.32 ± 0.27	-0.31 ± 0.36
S89 net TOA	-0.05 ± 0.40	-0.16 ± 0.41	-0.12 ± 0.43	0.09 ± 0.30
D19 net CRE	0.07 ± 0.29	0.00 ± 0.26	-0.22 ± 0.27	-0.05 ± 0.36
S89 net CRE	0.07 ± 0.40	0.17 ± 0.41	0.13 ± 0.43	0.25 ± 0.30

With the high uncertainty in both the net TOA balance and the net CRE for 1.35-seeding with both ice-cloud fraction approaches, plus the use of the unrealistic ice saturation threshold for full gridbox coverage for ice clouds in S89 (Section 3.1), we focus our comparison between 1.05-seeding and 1.35-seeding with D19 only. The global mean TOA radiative anomalies are

465 mostly inconclusive for both 1.05-seeding and 1.35-seeding. Therefore, we examine the zonal mean TOA anomalies for each seeding concentration for both $S_{i,seed}$ thresholds in Figure 8. The most striking finding from Figure 8 is that increasing $S_{i,seed}$ to 1.35 reduces the likelihood of overseeding, and, consistent with the TOA anomalies in Figure 3, even produces cooling for all seeding particle concentrations. For Seed100 with $S_{i,seed}$ = 1.05 (Figure 8a) the maximum positive TOA anomaly is around $13.0\,\mathrm{Wm^{-2}}$ in the southern hemisphere (SH) (not shown), whereas Seed100_1.35 (Figure 8b) the maximum positive radiative

470 forcing anomaly is less than $1.0\,\mathrm{Wm^{-2}}$. Remarkably, both $S_{i,seed}$ cases show small regions of negative forcing (i.e. a cooling effect), but for lower seeding particle concentrations. Seed0.1, Seed1, and Seed10 with $S_{i,seed}$ = 1.05 all show some degree of negative forcing around roughly $20\,°\mathrm{N}$, $45\,°\mathrm{N}$, and $70\,°\mathrm{N}$, whereas only Seed1 shows any appreciable negative forcing in the SH between $50\,°\mathrm{S}$ and $60\,°\mathrm{S}$, and Seed10 centered on $30\,°\mathrm{S}$. 1.35-seeding shows a similar negative forcing over wider areas centered around similar latitudes, but for all seeding particle concentrations. Both scenarios show very small negative forcing

475 in the tropics. The strongest cooling for 1.05-seeding of $-1.5\,\mathrm{Wm^{-2}}$ occurs for Seed1 around $20\,°\mathrm{N}$, and for 1.35-seeding around $-1.4\,\mathrm{Wm^{-2}}$ for Seed0.1_1.35 near the same latitude.

As Seed10_1.35 shows a small, but statistically significant cooling effect (Figure 3), plus wider areas of cooling evident in Figure 8, we investigate certainty of this zonal anomaly for both $S_{i,seed}$ scenarios with the 95 % confidence interval based on the variance of the five-year zonal data, as shown by the grey-shaded area in Figure 8. The uncertainty around specific latitudes

480 varies, with a wider 95 % confidence interval for both $S_{i,seed}$ scenarios towards higher latitudes in the northern hemisphere (NH). Seed10 does appear to lead to significant cooling around the same latitudes, $40\,°\mathrm{S}$ and $25\,°\mathrm{N}$ for both $S_{i,seed}$ scenarios, but the cooling is more evident and statistically significant with 1.35-seeding. The minimal cooling towards higher latitude regions contrasts previous findings (Storelvmo and Herger, 2014; Storelvmo et al., 2014). However, to examine these higher-latitude regions further, Table 4 presents the five-year mean net TOA anomalies between $60\,°\mathrm{N/S}$ and $90\,°\mathrm{N/S}$ as well as the 95 %

485 confidence interval around the mean. For 1.05-seeding, the strongest cooling occurs for Seed0.1 in the NH and for Seed1 in the
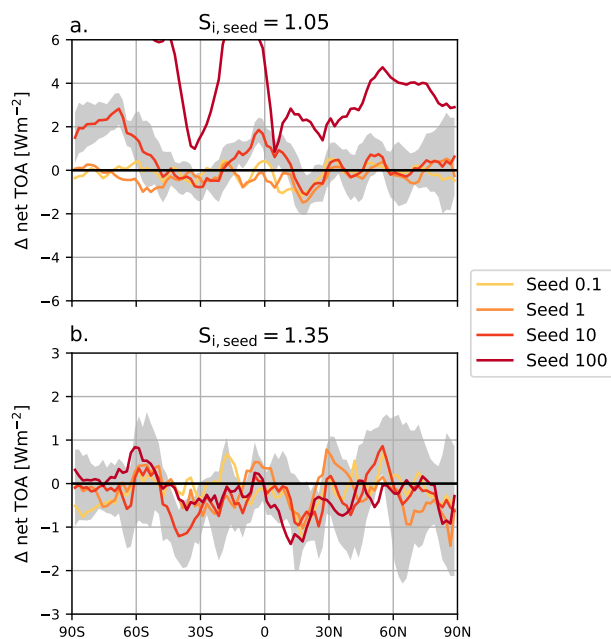
Figure 8. Five-year zonal mean net top-of-atmosphere (TOA) radiative balance anomalies between total SW and LW fluxes for a critical seeding particle saturation ratio of (a) 1.05 and (b) 1.35 for each seeding particle concentration minus the reference unseeded D19 simulation. The grey shaded area is the 95% confidence interval, representing the two-times standard deviation interval, of the Seed10 anomaly based on the variance of the five-year data.

SH. As shown previously, cooling occurs for all seeding particle concentrations for 1.35-seeding, except for Seed100_1.35 in the SH, with the strongest cooling for Seed1_1.35 in the NH. However, the uncertainty for seeding particle concentrations for both $S_{i,seed}$ scenarios is much higher than the mean TOA anomalies. Therefore, our results in this case only partially support the idea of an optimal seeding particle concentration around 1 INP L^{-1} (Gasparini and Lohmann, 2016). Furthermore, our

490 results cannot confirm the findings that higher latitude regions are the most desirable for CCT implementation (Storelvmo and Herger, 2014; Storelvmo et al., 2014; Gruber et al., 2019), as the net zonal TOA anomalies are rather uncertain.

We compare the zonal mean in-situ ice tracer anomalies for Seed10 and Seed10_1.35 in Figure 9 as this case showed statistically significant cooling for 1.35-seeding. Homogeneously-nucleated ice number anomalies within the cirrus regime (above the $238\,\mathrm{K}$ isotherm, dashed line in Figure 9) in both 1.05-seeding and 1.35-seeding cases appear to overlap to some

495 extent with the latitude bands that showed negative forcing anomalies in Figure 8. Seeding in these regions appears to lead to the desired shutting off of homogeneous nucleation. The signal is clearer in the in-situ heterogeneous tracer anomaly where positive values are much more wide spread for 1.05-seeding than 1.35-seeding. Heterogeneous nucleation increases by more than $10\,L^{-1}$ in most regions for 1.05-seeding, and to a lesser extent with 1.35-seeding. The latter shows higher uncertainty in the response, which points to the difference in ice nucleation competition between the two cases. With the former, we find

500 a similar situation as before, where heterogeneous nucleation on dust is overtaken by heterogeneous nucleation on seeding

Table 4. Five-year annual mean net top-of-atmosphere total radiative balance (TOA) in the Northern and Southern Hemispheres between $60\,°N/S$ and $90\,°N/S$ for D19 for seeding with a critical ice saturation ratio of 1.05 and 1.35. Each quantity includes the $95\,\%$ confidence interval equating to two standard deviations of the mean values of the five-year data.

Hemisphere	$S_{i,seed}$	Seed0.1	Seed1	Seed10	Seed100
Northern	1.05	-0.13 ± 1.12	-0.04 ± 1.28	0.16 ± 0.94	3.63 ± 1.73
Southern		-0.04 ± 0.67	-0.09 ± 0.82	2.13 ± 0.76	9.85 ± 1.73
Northern	1.35	-0.15 ± 0.89	-0.62 ± 1.17	-0.31 ± 1.06	-0.25 ± 0.72
Southern		-0.41 ± 0.60	-0.18 ± 0.71	-0.16 ± 0.50	0.22 ± 0.51

particles. For Seed10 this switch to seeding-particle-dominant heterogeneous nucleation within cirrus clouds appears to lead to a small positive TOA effect (Figure 3 and Table 2). We find the opposite TOA response with Seed10_1.35. Seeding particles in this case appear to shut off heterogeneous nucleation on mineral dust between roughly $45\,°N/S$. On the other hand, the amount of dust-driven nucleation increases towards higher latitudes. However, both homogeneous and heterogeneous nucleation ice

505 tracers for 1.35-seeding contain high uncertainty as shown by the stippling in Figure 9. The seeding ice tracer anomaly is more certain and shows increases of more than $10\,L^{-1}$ in the tropics, but is much less widespread than the 1.05-seeding scenario. This is due to the fact that a S_i of 1.35 occurs much less often in the atmosphere than a S_i of 1.05. Therefore, seeding particles with a higher $S_{i,seed}$ are much less efficient in this case at consuming water vapor to overtake other nucleation modes like in the 1.05-seeding scenario, leading to the insignificant zonal ice tracer anomalies, despite a clear significant positive anomaly

510 of heterogeneous nucleation on seeding particles.

  The uncertainty in the ICNC tracer anomalies for 1.35-seeding makes it difficult to understand the physical responses to a higher $S_{i,seed}$, despite some evidence of a regional sensitivity to seeding particles (Figure 8). In addition, previous studies suggested that CCT contains seasonal sensitivity (Storelvmo and Herger, 2014; Storelvmo et al., 2014) that we have not captured in our annual mean analysis to this point, which may be dampening a signal in our results. To address this, we examine

515 seasonal differences in zonally averaged TOA radiative flux anomalies in Figure 10 for the four seeding particle concentrations for 1.35-seeding. The net TOA (i.e. the balance between SW and LW) is presented in the first column for NH winter (top) and summer (bottom), with the SW and LW flux anomalies in the second and third columns respectively. Uncertainty is plotted around the Seed10_1.35 mean anomaly. A clear seasonal pattern is difficult to decipher from the TOA anomalies, except that in the NH seeding appears to lead to the desired cooling only during summer. Due to the negligible SW flux at high latitudes

520 during winter, the net TOA response is entirely driven by LW anomalies. Our model suggests that seeding particles act to enhance the already large LW CRE in this region (roughly $10.0\,Wm^{-2}$ around $75\,°N$ in the unseeded case) to produce only positive TOA anomalies. However, the uncertainty is high in Figure 10. During NH summer it appears that seeding particles act to enhance the SW CRE, as noted by the negative TOA SW anomalies in Figure 10, which outweighs the small positive LW anomalies. In fact, we find that the SW CRE in the unseeded reference case greatly exceeds the LW CRE between $60\,°N$ and

525 $90\,°N$ during this period. Thicker in-situ cirrus clouds in this case may contain some SW compensation as a result of seeding,
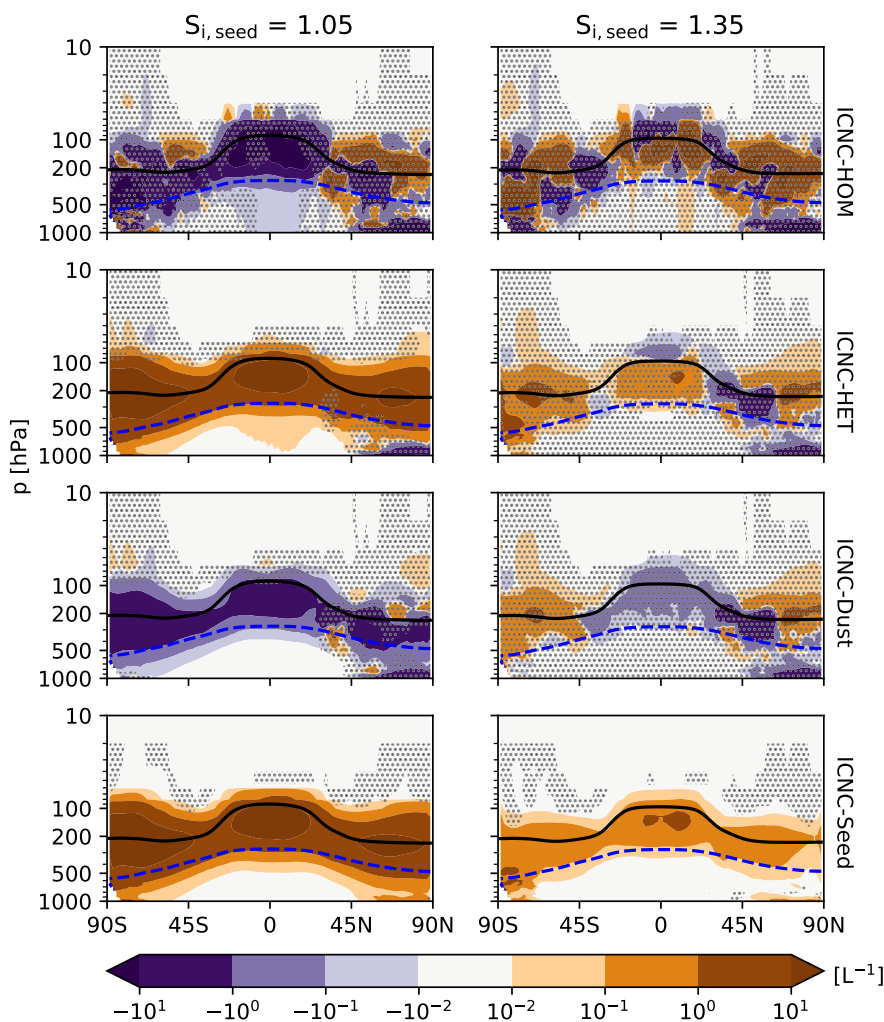
Figure 9. Five-year zonal mean ice number tracer $[\text{L}^{-1}]$ differences between the Seed10 simulation and the unseeded reference case D19 for seeding particle critical saturation ratios 1.05 (left) and 1.35 (right). The top row is the difference for in-situ homogeneously-nucleated ice number, the second row is the difference for the in-situ heterogeneous number, the third row is the difference for the heterogeneously-nucleated ice number formed on mineral dust particles, and the last row is the difference for the heterogeneously-nucleated ice number formed on seeding particles. The black line is the five-year mean zonal mean WMO-defined tropopause height on pressure levels, and the blue dashed line is the 238 K temperature contour. The stippling in the difference plots shows insignificant data points on the 95 % confidence level according to the independent t-test controlled by the "false discovery rate" method.

similar to the Twomey effect for lower-lying liquid or mixed-phase clouds (MPCs). This is somewhat in line with findings by Krämer et al. (2020), however we do not find evidence of a cirrus altitude shift to lower levels that could reduce their warming effect.
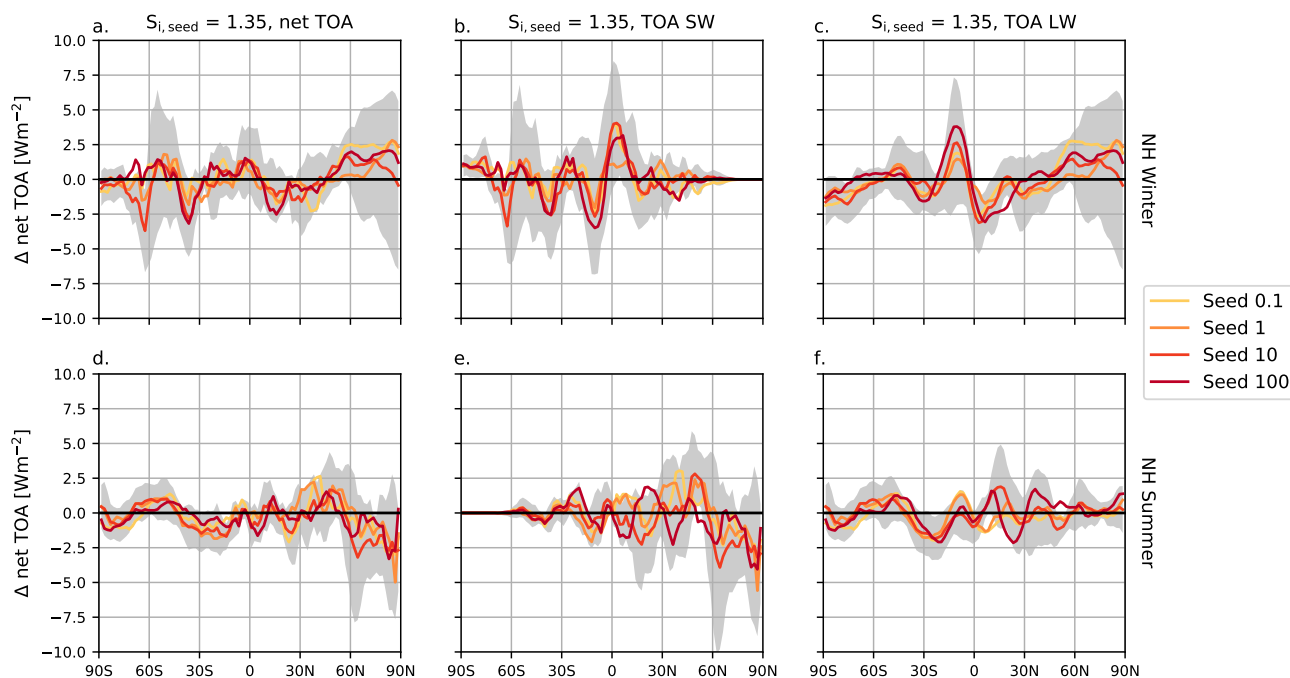
Figure 10. 1.35-seeding zonal mean radiative balance anomalies for all seeding particle concentrations for the net TOA (a,d), the TOA SW (b,e), and TOA LW (c,f). The top row shows the four-year zonal mean for NH winter (December - February) and the bottom row is the five-year zonal mean for NH summer (June - August). The grey shaded area is the $95\,\%$ confidence interval around the mean Seed10 anomaly, representing the two-times standard deviation interval, based on the variance of the annual data.

A more likely explanation is that 1.35-seeding impacts lower-lying mixed-phase clouds. Figure 11 shows the vertical profiles
530   of IWC and LWC anomalies for each seeding particle concentration, like in Figure 7 but for 1.35-seeding. Unexpectedly, we find that 1.35-seeding does not impact IWC within the cirrus regime, and leads to only very small positive anomalies in the mixed-phase regime. Instead LWC for the Seed10_1.35 case increases in the lowermost part of the mixed-phase regime by around $0.5\,\mathrm{mg\,m^{-3}}$, and even more so in the liquid phase. The lack of an IWC response, combined with the increase in heterogeneously nucleated ice on seeding particles and to some extent on mineral dust for Seed10_1.35, indicates that seeding
535   impacts the size of ice crystals, which in turn affects sedimentation from the cirrus regime. Ice crystal size anomalies are highly uncertain for the 1.35-seeding case (not shown), but indicate smaller ice crystals by about $1.0\,\mathrm{\mu m}$ throughout the cirrus regime. It is therefore likely that seeding particles in this case partially compensate the loss of ice formed on mineral dust in the tropics, and contribute to more numerous ice crystals in the extra-tropics (Figure 9) to form smaller ice crystals that weaken the sedimentation flux into the mixed-phase regime. The lack of large ice crystals in the mixed-phase regime, reduces cloud droplet
540   consumption via the WBF process or riming, and increases LWC. Lower-lying clouds with a higher LWC likely contribute to the strengthening of the SW CRE.
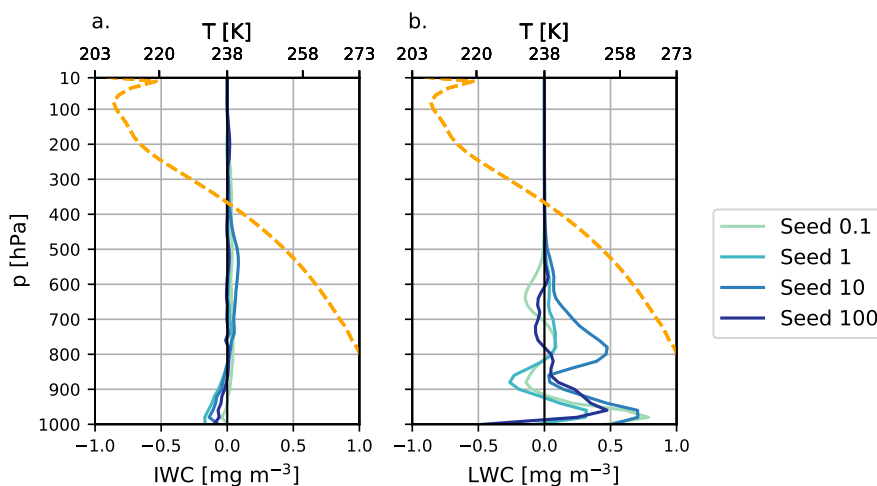
Figure 11. Five-year annual global mean (a) IWC and (b) liquid water content anomaly profiles as in Figure 7, but for $S_{i,seed} = 1.35$.

We also find summer cooling as a result of seeding in the SH (Figure 10a). Seed10_1.35 also produces a net cooling effect of more than $-2.5\,\mathrm{Wm^{-2}}$ around $60\,°\mathrm{S}$ that is driven mostly be a weaker TOA SW flux. This behavior is in direct contrast with previous findings by Storelvmo and Herger (2014); Storelvmo et al. (2014) who found that high latitude regions during winter were more susceptible to seeding to produce strong cooling effects. The lack of a cooling response in our model during NH winter highlights the high annual variability of cirrus cloud properties, which may be driven by large fluctuations of annual mean dust concentrations from the larger dust sources in the NH. The only appreciable wintertime cooling we find is in the SH (bottom row of Figure 10) where seeding produces cooling in a small region around $80\,°\mathrm{S}$ driven by an enhanced TOA LW flux. We reiterate here, however, that the seasonal, zonal mean TOA flux anomalies are surrounded by wide $95\,\%$ confidence intervals at high latitudes, therefore making the response uncertain.

3.4 Stratospheric Effects

So far our analysis focused on the changes in the troposphere leading to the TOA overseeding presented in Figure 3. However, our findings also point to stratospheric effects as a results of seeding, particularly the positive ICNC anomalies in the lower stratosphere (Figure 5) and the subsequent cloud fraction increase (Figure 4). The former can be partially explained by the seeding strategy we utilize in our cirrus scheme. Seeding particles are available in every gridbox of the cirrus scheme up to the $100\,\mathrm{hPa}$ pressure level. This places some of our seeding particles firmly within the troposphere in the tropics, but in the lower stratosphere in the mid and high latitudes. Therefore, seeding particles are present in environments with little competition between mineral dust (i.e. low INP environments) or liquid sulphate particles, leading to wide extents of the lower stratosphere with large positive ICNC anomalies. Cloud fraction increases accordingly with larger ice crystal number concentrations from

560   seeding. This effect is more widespread with S89 than D19 due to the ice saturation threshold for full gridbox coverage of ice

clouds used in the former.

    What remains unclear is the positive in-situ homogeneously-nucleated ice number anomaly in the mid-latitudes and towards

the poles in the lower stratosphere (Figure 6, top panel), and the higher cloud fractions that extend to pressure levels less

than $100\,\mathrm{hPa}$ (i.e. at higher altitudes). As both cloud fraction approaches are relative humidity based, the patterns observed in

565   stratospheric cloud fraction indicate a dynamic response to the INP perturbations by increasing temperature and consequently

enhancing upwelling of water vapor into the stratosphere from the tropical troposphere as shown in Figure 12. The anomalies

for lower seeding concentrations and for all simulations with a $S_{i,seed}$ of 1.35 are insignificant according to the FDR method.

Here, we only present the anomalies at pressure levels lower than $300\,\mathrm{hPa}$ (higher altitudes) to focus on the effects in the upper

troposphere and the stratosphere.

570   Overseeding in Seed100 leads to a positive temperature anomaly of more than $4\,\mathrm{K}$ in the tropical troposphere (Figure 12a).

As a result of warmer temperatures, the saturation specific humidity increases. Therefore, the specific humidity can increase

as well (Figure 12b). This appears to enhance water vapor upwelling into the lower stratosphere from the tropical troposphere,

as indicated by the positive specific humidity anomaly above the tropopause (Figure 12b) that also extends into the middle

stratosphere. Water vapor in the stratosphere has a cooling effect (Rind and Lonergan, 1995), as indicated by the temperature

575   response above the tropopause in the tropics and between $45\,\mathrm{°N/S}$ and $90\,\mathrm{°N/S}$. In the same region, updraft velocities increase

by more than $0.2\,\mathrm{cm\,s^{-1}}$. As we observe larger ice-cloud fractions in this region (Figure 4), enhanced LW cloud-top cooling

likely fuels the observed positive updraft anomaly. We find LW-cooling in the tropics in upper troposphere and in the extra-

tropics in the stratosphere in Figure 13. The latter is likely due to the positive water vapor anomaly in the lower stratosphere

(Figure 12b). At lower levels we find LW warming, likely caused by more trapping from more frequent and optically thicker

580   cirrus clouds. The increase in updraft velocity, in combination with the positive specific humidity anomaly, not only allows

the seeding particles to form abundant ice particles, but also allows air parcels to reach the critical saturation for homogeneous

nucleation. There are also small areas in the lower stratosphere where the anomaly of ice formed heterogeneously on mineral

dust particles is positive (Figure 6). This enhancement of natural ice formation processes at lower levels in the stratosphere

in response to overseeding in the troposphere (Section 3.1), plus the widespread positive anomaly of ice formed on seeding

585   particles in the same region leads to a higher abundance of clouds that likely contribute to the overall TOA warming effect

(Figure 3).

    The temperature anomaly presented in Figure 12a is not restricted to the lower stratosphere where we find enhanced ice

formation, which indicates that seeding could impact the wider stratosphere as a whole via a dynamic feedback on the Brewer-

Dobson Circulation (BDC), (Butchart and Scafie, 2001; Rind et al., 2001; Butchart et al., 2006; Butchart, 2014). The BDC

590   describes the global mass transport from the troposphere into the stratosphere, where air rises in the tropics and descends over

higher latitudes. One of the main findings following numerous studies on greenhouse-gas driven climate change is a speeding

up of this overturning circulation, with enhanced tropical mass upwelling, leading, in general, to a cooler stratosphere and a

warmer troposphere (Butchart, 2014). Calvo et al. (2010) studied the enhancement of gravity wave-fueled tropical upwelling

into the stratosphere during warm El Niño-Southern Oscillation (ENSO) events. They found that during such events tropo-
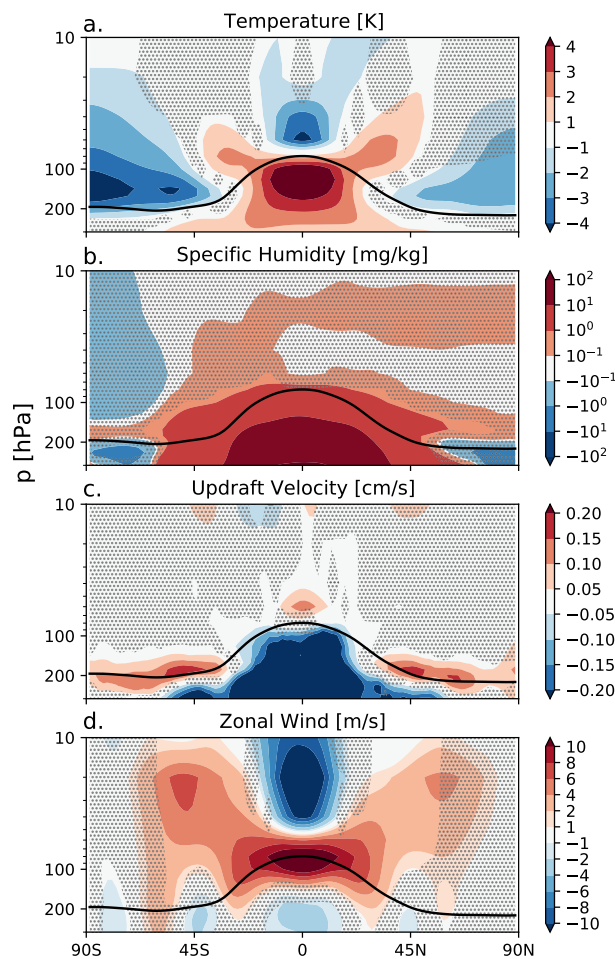
Figure 12. Five-year zonal mean (a) temperature, (b) specific humidity (c) updraft velocity, and (d) zonal wind anomalies for D19 with a seeding particle concentration of 100 INP L^{-1}. Anomalies are only shown for the upper troposphere and the stratosphere between $300\,\mathrm{hPa}$ and $10\,\mathrm{hPa}$. The black line is the five-year mean zonal mean WMO-defined tropopause height on pressure levels. The stippling in the difference plots shows insignificant data points on the $95\,\%$ confidence level according to the independent t-test controlled by the "false discovery rate" method.

595 spheric warming paired with tropical stratospheric cooling enhances the meridional temperature gradient. This strengthens the subtropical-jet, as seen by the increase in the zonal mean zonal wind, which is proportional to enhanced gravity wave drag forcing that fuels increased tropical upwelling (Calvo et al., 2010). Our results show a similar response with the positive temperature anomaly in the tropical tropopause (Figure 12a) that subsequently intensifies the sub-tropical jet, which we diagnosed from the zonal mean zonal wind anomaly in Figure 12d. The updraft anomaly in Figure 12c on the one hand shows a negative

600 updraft anomaly in the troposphere as a result of enhanced atmospheric stability due to a warmer upper troposphere, similar
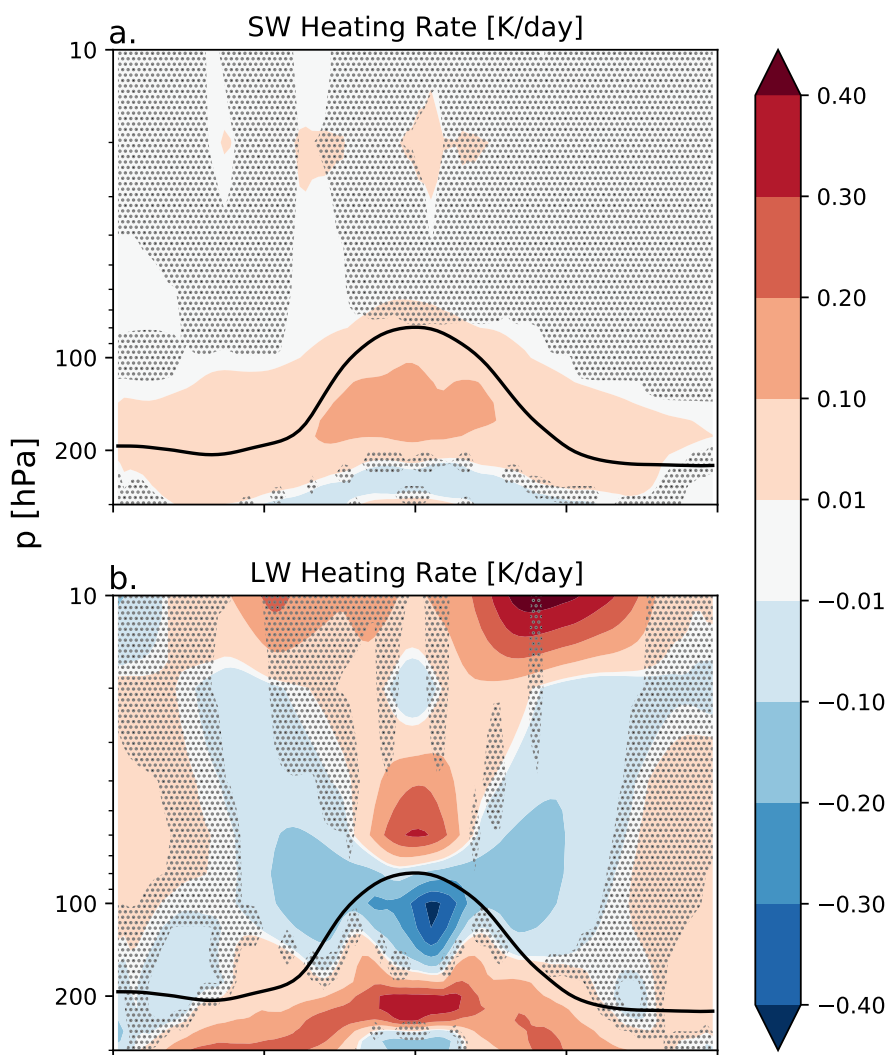
Figure 13. Five-year zonal mean (a) SW, and (b) LW heating rate anomalies for D19 with a seeding particle concentration of $100 \, \mathrm{INP \, L^{-1}}$. Anomalies are only shown for the upper troposphere and the stratosphere between $300 \, \mathrm{hPa}$ and $10 \, \mathrm{hPa}$. The black line is the five-year mean zonal mean WMO-defined tropopause height on pressure levels. The stippling in the difference plots shows insignificant data points on the $95 \, \%$ confidence level according to the independent t-test controlled by the "false discovery rate" method.

to the stabilization found by Kuebbeler et al. (2012) following stratospheric sulphur injections. On the other hand the positive updraft anomaly indicates a small enhancement of tropical upwelling in the stratosphere that would indicate a strengthening of the BDC. However, with this effect, the downward branch of the BDC leads to stronger warming in the stratosphere at higher latitudes (see Figure 6 from Calvo et al. (2010)) due to adiabatic compression. Our results show a negative temperature anomaly

605 at high latitudes in contrast to BDC-enhancement findings, rather pointing to a weakening of the downward branch. Instead, our results point to enhanced radiative cooling of the lower stratosphere in response to positive specific humidity anomalies.

4 Discussion

The results we presented in this study highlight a few important factors governing the sensitivity of CCT, namely, the approach for calculating ice-cloud fractions, the representation of stratiform ice microphysics, and the choice of $S_{i,seed}$ for ice nucleation

610 to occur on seeding particles. Our results also show the potential for unwanted side-effects of CCT on mixed-phase clouds and in the stratosphere.

In a first step, we tested the sensitivity of CCT between the original approach in ECHAM-HAM for calculating cloud fractions by Sundqvist et al. (1989), (S89) and the updated approach by Dietlicher et al. (2018, 2019), (D19). Overall we found that the D19 scheme reduces net TOA warming (i.e. the positive radiative forcing) by a factor of more than two for

615 Seed100 compared to S89 (Figure 3). Similar to the findings by Gasparini and Lohmann (2016), more frequent ice formation on seeding particles in our simulations led to cirrus cloud formation in previously cloud-free regions, using both ice-cloud fraction approaches, that was especially evident with the low $S_{i,seed}$ of 1.05. The conceptual difference between the two cloud fraction approaches can explain why positive cloud fraction anomalies were not as large with D19 than S89. With S89, the ice saturation threshold for full gridbox coverage of cirrus clouds meant that more frequent ice formation on seeding particles in

620 ice supersaturated conditions artificially expanded cloud fractions to unity, increasing the zonal average cloud fraction by more than 12%. On the other hand, while the reduction of homogeneous nucleation with D19 (Figure 6) reduced the frequency of fully covered grid boxes, the increase of heterogeneous nucleation on seeding particles increased the fractional cloud cover. Therefore, while both approaches showed a positive radiative effect as a result of seeding, D19 responses are lower because ice formation at a supersaturation suitable for heterogeneous nucleation on seeding particles does not induce as high cloud

625 fractions as in S89. This highlights limitations in both approaches for calculating ice cloud fractions. Where S89 artificially expanded ice-cloud fractions upon ice formation at supersaturation with respect to ice, ice-cloud fractions using D19 might be artificially low following seeding due to the criterion for full gridbox ice-cloud coverage only reached at homogeneous nucleation conditions. These limitations have wider implications on the radiative transfer calculations used to calculate TOA fluxes. The prognostic cloud scheme by Muench and Lohmann (2020) that explicitly calculates variables for cloud-free and

630 cloudy air, including in-cloud water vapor, could be used to overcome some of the limitations of the RH-based approaches, S89 and D19, and investigate cloud-fraction sensitivity to seeding particles.

Compared to CCT studies using the same model, ECHAM-HAM (Gasparini and Lohmann, 2016; Gasparini et al., 2017, 2020), we found much higher positive net TOA anomalies in response to seeding. For example, Gasparini and Lohmann (2016) followed a globally uniform seeding strategy using particles with radii of $0.5\,\mu m$ and $S_{i,seed} = 1.05$, like in our study here. In

635 their "Full" cirrus ice nucleation competition simulation (Section 2), they found a positive net TOA anomaly of $0.5\,Wm^{-2}$ when seeding with $100\,INP\,L^{-1}$, whereas we found $9.0\,Wm^{-2}$ with the same, S89, ice-cloud fraction approach. Results using our updated ice-cloud fraction approach, D19, were also an order of magnitude larger ($4.3\,Wm^{-2}$) than those by Gasparini

and Lohmann (2016) for the same seeding particle concentration. In addition, our Seed100 results were 16% and 143% larger, for D19 and S89 respectively, than the latest available IPCC forcing estimate of $3.7\,\mathrm{Wm}^{-2}$ from a doubling atmospheric CO_2

640 (Flato et al., 2013; Myhre et al., 2017).

The differences between our results to those by Gasparini and Lohmann (2016) point to differences in the in-situ cirrus scheme (Kärcher et al., 2006, Kuebbeler et al., 2014, Muench and Lohmann 2020, Kärcher and Marcolli 2021) and the treatment of ice microphysics (P3: Morrison and Milbrandt 2015, Dietlicher et al., 2018, 2019 versus 2M: Lohmann et al., 2007). In this study we updated the scaling of available aerosols for each freezing mode in the cirrus scheme, excluding dust deposition

645 modes as detailed below, by the fraction of ice in each nucleation mode from the previous timestep out of the total amount of stratiform pre-existing ice (Section 2). We deem this approach as more accurate than the previous approach to scale the available aerosols by the total amount of pre-existing ice. In a series of tests (not shown) we found that the updated scaling generated more heterogeneously-nucleated ice that only slightly decreased the amount of homogeneously-nucleated ice. The overall impact of the updated scaling did produce more in-situ ice from the cirrus scheme, but did not greatly alter ice nucle-

650 ation competition. As such, we do not attribute the majority of the differences in our results to previous CCT studies to the scaling changes of available aerosol in each nucleation modes in the cirrus scheme.

We also introduced the new differential activated fraction approach (Kärcher and Marcolli, 2021) with INP-budgeting for the dust deposition modes in the cirrus scheme. This approach no longer overestimates the amount of heterogeneous nucleation via deposition in each cirrus model timestep. Separate sensitivity tests (not shown) showed that this led to more homogeneously

655 nucleated in-situ cirrus ice, inferring a higher CCT efficacy. However, despite some evidence of cooling likely linked to rapid cloud adjustments rather than seeding, our results still differ greatly from those by Gasparini and Lohmann (2016); Gasparini et al. (2017).

It is more likely that our results differ to previous CCT studies due to the updated approach to represent ice as a single prognostic category in the microphysics scheme (P3, Dietlicher et al., 2018, 2019), as opposed to the size-separation approach

660 of in-cloud ice and snow (2M, Lohmann et al., 2007) in earlier versions of the model. The single category approach with P3 is achieved by a prognostic treatment of sedimentation, whereby this process is calculated as a vertical transport tendency based on the total ice particle size distribution (PSD). Ice removal is represented in a much more realistic way than in the 2M scheme, in which only a part of the ice PSD could fall. With the 2M scheme, as soon as ice grows larger than a certain threshold size it is converted to the snow category and falls out of the atmosphere in a single model timestep. In order to maintain realistic

665 cloud IWC values in the 2M scheme compared to observations, and to compensate for the unrealistic ice saturation threshold approach employed by the S89 cloud-fraction scheme, ice removal via snow formation was artificially enhanced by converting more cloud ice to snow. This was achieved by setting the tuning parameter for snow formation via ice crystal aggregation to an artificially high value ($\gamma_s = 900$, Neubauer et al., 2019; Dietlicher et al., 2019). This is no longer the case with the P3 scheme coupled to D19. A consequence of the slower and more realistic ice removal is that the ice crystal aggregation tuning

670 parameter is no longer relevant (Table 2, Dietlicher et al., 2019). Instead, ice crystal removal via larger crystals is augmented by an ice self-collection tuning parameter that is set to 6.0 (Section 2.1). Overall this means that ice in P3 remains in the atmosphere for a longer period of time. As a result, when seeding particles are introduced as additional INPs with P3, the

more numerous and smaller ice crystals we found (Figure 5 and Figure 6) do not necessarily grow into snow-sized ice particles and quickly sediment. This explains why we found much higher TOA radiative responses to seeding in this study compared to
675   Gasparini and Lohmann (2016); Gasparini et al. (2017). We argue, these previous CCT studies that did not include a prognostic representation of ice sedimentation likely underestimated the overseeding response as ice was removed too readily.

Another striking result from our study was the sensitivity of our model to the choice of $S_{i,seed}$. In a separate test, we increased $S_{i,seed}$ from 1.05 to 1.35 in an attempt to avoid impacts on heterogeneous nucleation on mineral dust particles, and only target homogeneous nucleation of liquid sulphate aerosols. Our results to some extent confirmed this hypothesis. 1.35-seeding led
680   to drastic net TOA reductions on a global-scale (Figure 3) and zonally (Figure 8) compared to 1.05-seeding. The cooling we found over a broad range of seeding particle concentrations with 1.35-seeding highlights that our model is less sensitive to an optimal seeding particle concentration like in previous findings (Storelvmo et al., 2013; Gasparini and Lohmann, 2016). This is a promising finding as obtaining precise seeding particle concentrations in a potential real-world setting would be difficult. The net TOA reductions we found with 1.35-seeding were also confirmed by the zonal ICNC tracer anomalies (Figure 9). For
685   1.35-seeding, seeding particles were much less effective at overtaking other nucleation modes.

We found only small regions of negative forcing in both the northern and southern hemispheres for both $S_{i,seed}$ cases, which to some extent compounds our understanding of certain regions being more susceptible to seeding (Storelvmo and Herger, 2014; Storelvmo et al., 2014). In the 1.05-seeding case, Seed1 led to a global-mean net TOA reduction of nearly $-0.4\,\mathrm{W\,m^{-2}}$. This concentration is similar to the optimal seeding concentration found by Gasparini and Lohmann (2016), whose results showed
690   a global net TOA reduction of $-0.3\,\mathrm{W\,m^{-2}}$. However, the total ICNC anomalies (Figure 5) in our model are uncertain in this case, as well as the net TOA response towards high latitude regions (Table 4). Perhaps a more interesting result is the 1.35-seeding case, where we found noticeable TOA forcing reductions for all seeding particle concentrations zonally (Figure 8). As the Seed10_1.35 net TOA anomaly was the only statistically negative response, we examined this case in more detail seasonally in Figure 10. Based on that analysis, our results do not extend findings by Storelvmo and Herger (2014) and Storelvmo et al.
695   (2014) that high-latitude wintertime seeding is an effective strategy. In our model, seeding amplifies the already large cirrus LW CRE in such regions to produce large net TOA warming. Instead, our model points to small regions of summertime cooling as a result of seeding, by enhancing the SW CRE, likely from adjustments in lower-lying mixed-phase and liquid clouds. This may be caused by the longer ice residence times within clouds with the P3 scheme, which impacts ice sedimentation into the mixed-phase regime. Overall, our results indicate that more thorough investigations of targeted seeding within high latitude
700   regions are needed for future work. Furthermore, our results likely point to a trade-off when pursuing further CCT studies: increasing $S_{i,seed}$ is likely an attractive alternative to avoid wide nucleation competition alterations as seen with lower $S_{i,seed}$, however, the scale to which seeding particles could produce the desired cooling effect remains to be examined with more detailed regional analyses.

Our results underscore the need for an investigation into a feasible $S_{i,seed}$, instead of using a somewhat arbitrary value as was
705   used in previous CCT studies. Seeding particles were simulated to nucleate ice as a threshold freezing process in our model (Section 2), meaning all aerosol particles within the mode that were available in any given gridbox would nucleate ice upon the right conditions being met. In the 1.05-seeding case this meant that seeding particles would nucleate ice at a relatively low S_i

relative to the other nucleation modes, enhancing their ability to overtake other processes and easily produce a strong positive forcing from overseeding (Figure 6 and Figure 9). The results were less clear in the 1.35-seeding case, with mixed responses

710 throughout the troposphere, which means defining an exact microphysical response is unclear. However, it is clear from our study that the choice of $S_{i,seed}$ is an important factor in determining CCT efficacy. Therefore, more detailed investigations of specific seeding particle materials and their ice-nucleating ability, perhaps in line with the continuous freezing process in this study (Section 2), is also needed in order to move CCT studies in line with potential real-world application.

Finally, the potential side effects of CCT were only starting to be investigated within the last few years (Lohmann and

715 Gasparini, 2017). In high resolution simulations Gruber et al. (2019) found that CCT not only resulted in thinner cirrus clouds, but also the larger ice particles formed by heterogeneous nucleation on seeding particles acted to reduce lower-lying MPCs through enhanced riming and ice crystal growth via the WBF process. The combination of these two effects resulted in a net TOA cooling effect. Gasparini et al. (2017) also found impact on lower-lying clouds in their simulations using increased sedimentation velocity as a proxy for CCT with seeding particles, following Muri et al. (2014). The "redistribution" of ice to

720 lower-lying MPCs counteracted cooling from reduced cirrus cloud fractions in their sedimentation simulations. In their CCT simulations using seeding INPs, they also found an MPC feedback, resulting from increased convective activity drying the lower troposphere that led smaller MPC fractions. As noted above, our results also showed a sedimentation flux reduction, but we also found a reduction in convective activity due to LW warming by a maximum of roughly $0.7\,\mathrm{K/day}$ (not shown) for D19 Seed100, which led to tropospheric stabilization (Figure 12). However, our results do not show significant cloud

725 fraction anomalies in the mixed-phase regime, and rather highlight that the weaker sedimentation flux explains the positive LWC anomaly as shown in Figure 7. MPCs with larger LWC led to stronger SW cooling, which was outweighed by warming from the increase of cirrus cloud fractions with smaller and more numerous ICs in the 1.05-seeding case.

5 Conclusions

We tested the sensitivity of CCT efficacy to the approach used for calculating ice cloud fractions and $S_{i,seed}$ using a new

730 physically-based representation of ice microphysics in the ECHAM-HAM GCM. We conclude with the following main findings:

1. Increasing the RH thresholds for the calculation of cirrus cloud fractions, reduces the positive forcing from overseeding by avoiding artificial cirrus cloud expansion upon ice nucleation.

2. The more realistic, prognostic treatment of sedimentation with the P3 microphysics scheme, leading to much slower

735 ice-removal than with the 2M scheme as in Gasparini and Lohmann (2016), likely means that responses to seeding are no longer underestimated. Rather, seeding in our model produces smaller and more numerous ice particles that amplify the already longer ice residence times within clouds to induce a strong positive TOA forcing.

3. Increasing $S_{i,seed}$ from 1.05 to 1.35 eliminates overseeding, indicating a broad range of seeding particle concentrations that increase the likelihood of producing a cooling response.

740   4. Globally CCT is unlikely to produce the desired cooling effects due to dynamic adjustments and background aerosol
        concentration heterogeneity. Instead, small regions centered around specific latitudes show only a small potential of
        targeted seeding.

      5. Our results do not support wintertime high-latitude seeding, contrasting Storelvmo and Herger (2014) and Storelvmo
        et al. (2014). We found small regions of cooling in the summer hemisphere that likely led to feedbacks on lower-lying
745   mixed-phase clouds, arguing that targeted seeding for specific regions or time periods should be further investigated in
        higher resolution modeling studies like the one by Gruber et al. (2019).

    The results presented in this study make a good case for testing the sensitivity of different seeding particle parameteriza-
tions. We showed that increasing $S_{i,seed}$ can lead to drastically different outcomes, limiting the potential for warming from
overseeding. We also showed that seeding with small particles appears undesirable as they lead to smaller ice particles fol-
750 lowing nucleation, reduced sedimentation fluxes, and longer-lived cirrus clouds. Gasparini et al. (2017) found seeding with
larger particles to lead to larger cooling that can somewhat offset CO_2-induced warming. In addition, the timing of seeding
particle injection is key so as to only seed regions prior to natural cirrus formation. This poses one of the largest uncertainties
for CCT, as forecasting cirrus formation is difficult with current techniques. On top of that, predicting where cirrus ice forms
predominantly via homogeneous nucleation will be a significant challenge.

755   Arguably, the abandonment of the size-dependent hydrometeor class separation approach with P3 can make the interpretation
of seeding impacts closer to first principles (Dietlicher et al., 2018). However, there are still large differences in the outcome of
CCT studies between the two leading climate models that to date were used to study CCT, ECHAM-HAM and CESM-CAM
(Storelvmo et al., 2014; Penner et al., 2015; Gasparini and Lohmann, 2016; Gasparini et al., 2017), regardless of a new ice
microphysics scheme. Such wide differences can be partially attributed to a lack of reliable in-situ observations of cirrus in
760 order to constrain models, though this gap is starting to be closed with more recent studies (Krämer et al., 2016; Krämer et al.,
2020). However, our results also extend the conclusion that a consistent approach among climate modeling groups on CCT
studies is needed (Gasparini et al., 2020), especially if the desire amongst the scientific community is to critically assess this
proposed method as a feasible climate intervention strategy.

    In line with the proposed real-world delivery mechanism of seeding particles using commercial aircraft (Mitchell and
765 Finnegan, 2009), there is a need to test the impact of aviation soot emissions on cirrus formation by including soot parti-
cles as potential INPs within the cirrus regime (e.g., Lohmann et al., 2020). Following on from that analysis, designing future
CCT studies to include aviation will more closely align modelling studies to potential implementation.

Code and data availability. The data for this study are available online at: https://doi.org/10.5281/zenodo.5091786 (Tully et al., 2021a). The
scripts used for post-processing the raw output data and producing the figures for this manuscript are available online at:
770 https://doi.org/10.5281/zenodo.5091772 (Tully et al., 2021b). In-situ measurement data were provided directly by Martina Krämer (m.kraemer@fz-
juelich.de).

Author contributions. Colin Tully, David Neubauer and Ulrike Lohmann designed the experiments. Colin Tully ran the model simulations, analysed the data, post-processing and plotting, and wrote the manuscript with comments from all co-authors. Nadja Omanovic contributed to the model development and the data analysis. Ulrike Lohmann and David Neubauer helped with the interpretation of the results.

775 *Competing interests.* The authors declare that they have no conflict of interest.

Acknowledgements. This Project is funded by the European Union under the Grant Agreement No. 875036. This work was supported by a grant from the Swiss National Supercomputing Centre (CSCS) under project ID s903. The authors would like to thank Martina Krämer for graciously providing the in-situ measurement data for model validation, Jörg Wieder for invaluable Python help to prepare the figures for this manuscript, Sylvaine Ferrachat for technical assistance running the model and analysing the data, Bernat Jiménez Esteve for providing
780 helpful advice for interpreting our results for discussion of stratospheric impacts, and Steffen Münch for helping to understand the cirrus scheme and for fruitful discussions on seeding particle implementation potential within the model.

References

Butchart, N.: The Brewer-Dobson circulation, Reviews of Geophysics, 52, 157–184, https://doi.org/10.1002/2013RG000448, https://agupubs.onlinelibrary.wiley.com/doi/abs/10.1002/2013RG000448, 2014.

Butchart, N. and Scafie, A.: Removal of chlorofluorocarbons by increased mass exchange between the stratosphere and troposphere in a changing climate, Nature, 410, 799–802, https://doi.org/https://doi.org/10.1038/35071047, https://www.nature.com/articles/35071047, 2001.

Butchart, N., Scafie, A., Bourqui, M., de Grandpré, J., Hare, S., Kettleborough, J., Langematz, U., Manzini, E., Sassi, F., Shibata, K., Shindell, D., and Sigmond, M.: Simulations of anthropogenic change in the strength of the Brewer–Dobson circulation, Climate Dynamics, 27, 727–741, https://doi.org/10.1007/s00382-006-0162-4, https://doi.org/10.1007/s00382-006-0162-4, 2006.

Calvo, N., Garcia, R. R., Randel, W. J., and Marsh, D. R.: Dynamical Mechanism for the Increase in Tropical Upwelling in the Lowermost Tropical Stratosphere during Warm ENSO Events, Journal of the Atmospheric Sciences, 67, 2331–2340, https://doi.org/10.1175/2010JAS3433.1, https://journals.ametsoc.org/view/journals/atsc/67/7/2010jas3433.1.xml, 2010.

Crutzen, P. J.: Albedo Enhancement by Stratospheric Sulfur Injections: A Contribution to Resolve a Policy Dilemma?, Climatic Change, 77, 2784–2786, https://doi.org/10.1007/s10584-006-9101-y, https://doi.org/10.1007/s10584-006-9101-y, 2006.

Cziczo, D. J., Froyd, K. D., Hoose, C., Jensen, E. J., Diao, M., Zondlo, M. A., Smith, J. B., Twohy, C. H., and Murphy, D. M.: Clarifying the Dominant Sources and Mechanisms of Cirrus Cloud Formation, Science, 340, 1320–1324, https://doi.org/10.1126/science.1234145, https://science.sciencemag.org/content/340/6138/1320, 2013.

Cziczo, D. J., Wolf, M. J., Gasparini, B., Münch, S., and Lohmann, U.: Unanticipated Side Effects of Stratospheric Albedo Modification Proposals Due to Aerosol Composition and Phase, Scientific Reports, 9, https://doi.org/10.1038/s41598-019-53595-3, https://doi.org/10.1038/s41598-019-53595-3, 2019.

DeMott, P. J., Cziczo, D. J., Prenni, A. J., Murphy, D. M., Kreidenweis, S. M., Thomson, D. S., Borys, R., and Rogers, D. C.: Measurements of the concentration and composition of nuclei for cirrus formation, Proceedings of the National Academy of Sciences, 100, 14 655–14 660, https://doi.org/10.1073/pnas.2532677100, https://www.pnas.org/content/100/25/14655, 2003.

DeMott, P. J., Prenni, A. J., Liu, X., Kreidenweis, S. M., Petters, M. D., Twohy, C. H., Richardson, M. S., Eidhammer, T., and Rogers, D. C.: Predicting global atmospheric ice nuclei distributions and their impacts on climate, Proceedings of the National Academy of Sciences, 107, 11 217–11 222, https://doi.org/10.1073/pnas.0910818107, https://www.pnas.org/content/107/25/11217, 2010.

Dietlicher, R., Neubauer, D., and Lohmann, U.: Prognostic parameterization of cloud ice with a single category in the aerosol-climate model ECHAM(v6.3.0)-HAM(v2.3), Geoscientific Model Development, 11, 1557–1576, https://doi.org/10.5194/gmd-11-1557-2018, https://gmd.copernicus.org/articles/11/1557/2018/, 2018.

Dietlicher, R., Neubauer, D., and Lohmann, U.: Elucidating ice formation pathways in the aerosol–climate model ECHAM6-HAM2, Atmospheric Chemistry and Physics, 19, 9061–9080, https://doi.org/10.5194/acp-19-9061-2019, https://www.atmos-chem-phys.net/19/9061/2019/, 2019.

Dykema, J. A., Keith, D. W., and Keutsch, F. N.: Improved aerosol radiative properties as a foundation for solar geoengineering risk assessment, Geophysical Research Letters, 43, 7758–7766, https://doi.org/https://doi.org/10.1002/2016GL069258, https://agupubs.onlinelibrary.wiley.com/doi/abs/10.1002/2016GL069258, 2016.

Flato, G., J., Marotzke, B., Abiodun, P., Braconnot, S., Chou, W., Collins, P., Cox, F., Driouech, S., Emori, V., Eyring, C., Forest, P., Gleckler, E., Guilyardi, C., Jakob, V., Kattsov, C., Reason, and Rummukainen, M.: Evaluation of Climate Models, Cambridge University Press, https://doi.org/10.1017/CBO9781107415324.020, 2013.

820   Gasparini, B. and Lohmann, U.: Why cirrus cloud seeding cannot substantially cool the planet, Journal of Geophysical Research: Atmospheres, 121, 4877–4893, https://doi.org/10.1002/2015JD024666, https://agupubs.onlinelibrary.wiley.com/doi/abs/10.1002/2015JD024666, 2016.

Gasparini, B., Münch, S., Poncet, L., Feldmann, M., and Lohmann, U.: Is increasing ice crystal sedimentation velocity in geoengineering simulations a good proxy for cirrus cloud seeding?, Atmospheric Chemistry and Physics, 17, 4871–4885, https://doi.org/10.5194/acp-17-4871-2017, https://acp.copernicus.org/articles/17/4871/2017/, 2017.

825   Gasparini, B., Meyer, A., Neubauer, D., Münch, S., and Lohmann, U.: Cirrus Cloud Properties as Seen by the CALIPSO Satellite and ECHAM-HAM Global Climate Model, Journal of Climate, 31, 1983–2003, https://doi.org/10.1175/JCLI-D-16-0608.1, https://doi.org/10.1175/JCLI-D-16-0608.1, 2018.

Gasparini, B., McGraw, Z., Storelvmo, T., and Lohmann, U.: To what extent can cirrus cloud seeding counteract global warming?, Environmental Research Letters, 15, 054 002, https://doi.org/10.1088/1748-9326/ab71a3, https://doi.org/10.1088%2F1748-9326%2Fab71a3, 2020.

830

Gruber, S., Blahak, U., Haenel, F., Kottmeier, C., Leisner, T., Muskatel, H., Storelvmo, T., and Vogel, B.: A Process Study on Thinning of Arctic Winter Cirrus Clouds With High-Resolution ICON-ART Simulations, Journal of Geophysical Research: Atmospheres, 124, 5860–5888, https://doi.org/10.1029/2018JD029815, https://agupubs.onlinelibrary.wiley.com/doi/abs/10.1029/2018JD029815, 2019.

835   Heymsfield, A. J., Krämer, M., Luebke, A., Brown, P., Cziczo, D. J., Franklin, C., Lawson, P., Lohmann, U., McFarquhar, G., Ulanowski, Z., and Van Tricht, K.: Cirrus Clouds, Meteorological Monographs, 58, 2.1–2.26, https://doi.org/10.1175/AMSMONOGRAPHS-D-16-0010.1, https://doi.org/10.1175/AMSMONOGRAPHS-D-16-0010.1, 2017.

Hoesly, R. M., Smith, S. J., Feng, L., Klimont, Z., Janssens-Maenhout, G., Pitkanen, T., Seibert, J. J., Vu, L., Andres, R. J., Bolt, R. M., Bond, T. C., Dawidowski, L., Kholod, N., Kurokawa, J.-I., Li, M., Liu, L., Lu, Z., Moura, M. C. P., O'Rourke, P. R., and Zhang, Q.: Historical
840   (1750–2014) anthropogenic emissions of reactive gases and aerosols from the Community Emissions Data System (CEDS), Geoscientific Model Development, 11, 369–408, https://doi.org/10.5194/gmd-11-369-2018, https://gmd.copernicus.org/articles/11/369/2018/, 2018.

Hong, Y., Liu, G., and Li, J.-L. F.: Assessing the Radiative Effects of Global Ice Clouds Based on CloudSat and CALIPSO Measurements, Journal of Climate, 29, 7651 – 7674, https://doi.org/10.1175/JCLI-D-15-0799.1, https://journals.ametsoc.org/view/journals/clim/29/21/jcli-d-15-0799.1.xml, 2016.

845   Ickes, L., Welti, A., Hoose, C., and Lohmann, U.: Classical nucleation theory of homogeneous freezing of water: thermodynamic and kinetic parameters, Phys. Chem. Chem. Phys., 17, 5514–5537, https://doi.org/10.1039/C4CP04184D, http://dx.doi.org/10.1039/C4CP04184D, 2015.

Jensen, E. J., Ueyama, R., Pfister, L., Bui, T. V., Alexander, M. J., Podglajen, A., Hertzog, A., Woods, S., Lawson, R. P., Kim, J.-E., and Schoeberl, M. R.: High-frequency gravity waves and homogeneous ice nucleation in tropical tropopause layer cirrus, Geophysical Research Letters, 43, 6629–6635, https://doi.org/10.1002/2016GL069426, https://agupubs.onlinelibrary.wiley.com/doi/abs/10.1002/2016GL069426, 2016a.

850

Jensen, E. J., Ueyama, R., Pfister, L., Bui, T. V., Lawson, R. P., Woods, S., Thornberry, T., Rollins, A. W., Diskin, G. S., DiGangi, J. P., and Avery, M. A.: On the Susceptibility of Cold Tropical Cirrus to Ice Nuclei Abundance, Journal of the Atmospheric Sciences, 73, 2445–2464, https://doi.org/10.1175/JAS-D-15-0274.1, https://doi.org/10.1175/JAS-D-15-0274.1, 2016b.

855 Joos, H., Spichtinger, P., and Lohmann, U.: Influence of a future climate on the microphysical and optical properties of orographic cirrus
clouds in ECHAM5, Journal of Geophysical Research: Atmospheres, 115, https://doi.org/https://doi.org/10.1029/2010JD013824, https:
//agupubs.onlinelibrary.wiley.com/doi/abs/10.1029/2010JD013824, 2010.

Kanji, Z. A., Ladino, L. A., Wex, H., Boose, Y., Burkert-Kohn, M., Cziczo, D. J., and Krämer, M.: Overview of Ice Nucleating Par-
ticles, Meteorological Monographs, 58, 1.1–1.33, https://doi.org/10.1175/AMSMONOGRAPHS-D-16-0006.1, https://doi.org/10.1175/
860 AMSMONOGRAPHS-D-16-0006.1, 2017.

Keith, D. W., Weisenstein, D. K., Dykema, J. A., and Keutsch, F. N.: Stratospheric solar geoengineering without ozone loss, Proceedings of
the National Academy of Sciences, 113, 14 910–14 914, https://doi.org/10.1073/pnas.1615572113, https://www.pnas.org/content/113/52/
14910, 2016.

Koop, T., Luo, B., Tsias, A., and Peter, T.: Water activity as the determinant for homogeneous ice nucleation in aqueous solutions, Nature,
865 406, 611–614, https://doi.org/10.1038/35020537, 2000.

Krämer, M., Rolf, C., Luebke, A., Afchine, A., Spelten, N., Costa, A., Meyer, J., Zöger, M., Smith, J., Herman, R. L., Buchholz, B., Ebert,
V., Baumgardner, D., Borrmann, S., Klingebiel, M., and Avallone, L.: A microphysics guide to cirrus clouds – Part 1: Cirrus types,
Atmospheric Chemistry and Physics, 16, 3463–3483, https://doi.org/10.5194/acp-16-3463-2016, https://acp.copernicus.org/articles/16/
3463/2016/, 2016.

870 Krämer, M., Rolf, C., Spelten, N., Afchine, A., Fahey, D., Jensen, E., Khaykin, S., Kuhn, T., Lawson, P., Lykov, A., Pan, L. L., Riese,
M., Rollins, A., Stroh, F., Thornberry, T., Wolf, V., Woods, S., Spichtinger, P., Quaas, J., and Sourdeval, O.: A microphysics guide
to cirrus – Part 2: Climatologies of clouds and humidity from observations, Atmospheric Chemistry and Physics, 20, 12 569–12 608,
https://doi.org/10.5194/acp-20-12569-2020, https://acp.copernicus.org/articles/20/12569/2020/, 2020.

Kuebbeler, M., Lohmann, U., and Feichter, J.: Effects of stratospheric sulfate aerosol geo-engineering on cirrus clouds, Geophysi-
875 cal Research Letters, 39, https://doi.org/https://doi.org/10.1029/2012GL053797, https://agupubs.onlinelibrary.wiley.com/doi/abs/10.1029/
2012GL053797, 2012.

Kuebbeler, M., Lohmann, U., Hendricks, J., and Kärcher, B.: Dust ice nuclei effects on cirrus clouds, Atmospheric Chemistry and Physics,
14, 3027–3046, https://doi.org/10.5194/acp-14-3027-2014, https://www.atmos-chem-phys.net/14/3027/2014/, 2014.

Kärcher, B. and Burkhardt, U.: A cirrus cloud scheme for general circulation models, Quarterly Journal of the Royal Meteorological Society,
880 134, 1439–1461, https://doi.org/https://doi.org/10.1002/qj.301, https://rmets.onlinelibrary.wiley.com/doi/abs/10.1002/qj.301, 2008.

Kärcher, B. and Lohmann, U.: A parameterization of cirrus cloud formation: Homogeneous freezing of supercooled aerosols, Journal of
Geophysical Research: Atmospheres, 107, AAC 4–1–AAC 4–10, https://doi.org/10.1029/2001JD000470, https://agupubs.onlinelibrary.
wiley.com/doi/abs/10.1029/2001JD000470, 2002.

Kärcher, B. and Lohmann, U.: A parameterization of cirrus cloud formation: Heterogeneous freezing, Journal of Geophysical Research: At-
885 mospheres, 108, https://doi.org/10.1029/2002JD003220, https://agupubs.onlinelibrary.wiley.com/doi/abs/10.1029/2002JD003220, 2003.

Kärcher, B. and Marcolli, C.: Aerosol-cloud interactions: The representation of heterogeneous ice activation in cloud models, At-
mospheric Chemistry and Physics Discussions, 2021, 1–11, https://doi.org/10.5194/acp-2021-511, https://acp.copernicus.org/preprints/
acp-2021-511/, 2021.

Kärcher, B., Hendricks, J., and Lohmann, U.: Physically based parameterization of cirrus cloud formation for use in global atmospheric
890 models, Journal of Geophysical Research: Atmospheres, 111, https://doi.org/10.1029/2005JD006219, https://agupubs.onlinelibrary.wiley.
com/doi/abs/10.1029/2005JD006219, 2006.

Levkov, L., Rockel, B., Kapitza, H., and Raschke, E.: 3D mesoscale numerical studies of cirrus and stratus clouds by their time and space evolution, Contributions to atmospheric physics, 65, 35–58, 1992.

Lohmann, U. and Diehl., K.: Sensitivity Studies of the Importance of Dust Ice Nuclei for the Indirect Aerosol Effect on Stratiform Mixed-Phase Clouds, Journal of the Atmospheric Sciences, 63, 968–982, https://doi.org/10.1175/JAS3662.1, https://doi.org/10.1175/JAS3662.1, 2006.

Lohmann, U. and Ferrachat, S.: Impact of parametric uncertainties on the present-day climate and on the anthropogenic aerosol effect, Atmospheric Chemistry and Physics, 10, 11 373–11 383, https://doi.org/10.5194/acp-10-11373-2010, https://acp.copernicus.org/articles/10/11373/2010/, 2010.

Lohmann, U. and Gasparini, B.: A cirrus cloud climate dial?, Science, 357, 248–249, https://doi.org/10.1126/science.aan3325, https://science.sciencemag.org/content/357/6348/248, 2017.

Lohmann, U. and Kärcher, B.: First interactive simulations of cirrus clouds formed by homogeneous freezing in the ECHAM general circulation model, Journal of Geophysical Research: Atmospheres, 107, AAC 8–1–AAC 8–13, https://doi.org/10.1029/2001JD000767, https://agupubs.onlinelibrary.wiley.com/doi/abs/10.1029/2001JD000767, 2002.

Lohmann, U., Stier, P., Hoose, C., Ferrachat, S., Kloster, S., Roeckner, E., and Zhang, J.: Cloud microphysics and aerosol indirect effects in the global climate model ECHAM5-HAM, Atmospheric Chemistry and Physics, 7, 3425–3446, https://doi.org/10.5194/acp-7-3425-2007, https://www.atmos-chem-phys.net/7/3425/2007/, 2007.

Lohmann, U., Spichtinger, P., Jess, S., Peter, T., and Smit, H.: Cirrus cloud formation and ice supersaturated regions in a global climate model, Environmental Research Letters, 3, 045 022, https://doi.org/10.1088/1748-9326/3/4/045022, https://doi.org/10.1088%2F1748-9326%2F3%2F4%2F045022, 2008.

Lohmann, U., Lüönd, F., and Mahrt, F.: An Introduction to Clouds: From the Microscale to Climate, Cambridge University Press, https://doi.org/10.1017/CBO9781139087513, 2016.

Lohmann, U., Friebel, F., Kanji, Z., Mahrt, F., Mensah, A., and Neubauer, D.: Future warming exacerbated by aged-soot effect on cloud formation, Nature Geoscience, 13, 674–680, https://doi.org/10.1038/s41561-020-0631-0, https://doi.org/10.1038/s41561-020-0631-0, 2020.

Mahrt, F., Marcolli, C., David, R. O., Grönquist, P., Barthazy Meier, E. J., Lohmann, U., and Kanji, Z. A.: Ice nucleation abilities of soot particles determined with the Horizontal Ice Nucleation Chamber, Atmospheric Chemistry and Physics, 18, 13 363–13 392, https://doi.org/10.5194/acp-18-13363-2018, https://acp.copernicus.org/articles/18/13363/2018/, 2018.

Mahrt, F., Kilchhofer, K., Marcolli, C., Grönquist, P., David, R. O., Rösch, M., Lohmann, U., and Kanji, Z. A.: The Impact of Cloud Processing on the Ice Nucleation Abilities of Soot Particles at Cirrus Temperatures, Journal of Geophysical Research: Atmospheres, 125, e2019JD030 922, https://doi.org/10.1029/2019JD030922, https://agupubs.onlinelibrary.wiley.com/doi/abs/10.1029/2019JD030922, e2019JD030922 10.1029/2019JD030922, 2020.

Mauritsen, T., Stevens, B., Roeckner, E., Crueger, T., Esch, M., Giorgetta, M., Haak, H., Jungclaus, J., Klocke, D., Matei, D., Mikolajewicz, U., Notz, D., Pincus, R., Schmidt, H., and Tomassini, L.: Tuning the climate of a global model, Journal of Advances in Modeling Earth Systems, 4, https://doi.org/https://doi.org/10.1029/2012MS000154, https://agupubs.onlinelibrary.wiley.com/doi/abs/10.1029/2012MS000154, 2012.

Mitchell, D. L. and Finnegan, W.: Modification of cirrus clouds to reduce global warming, Environmental Research Letters, 4, 045 102, https://doi.org/10.1088/1748-9326/4/4/045102, https://doi.org/10.1088%2F1748-9326%2F42F4%2F045102, 2009.

Mitchell, D. L., Rasch, P., Ivanova, D., McFarquhar, G., and Nousiainen, T.: Impact of small ice crystal assumptions on ice sedimentation rates in cirrus clouds and GCM simulations, Geophysical Research Letters, 35, https://doi.org/https://doi.org/10.1029/2008GL033552, https://agupubs.onlinelibrary.wiley.com/doi/abs/10.1029/2008GL033552, 2008.

Möhler, O., Field, P. R., Connolly, P., Benz, S., Saathoff, H., Schnaiter, M., Wagner, R., Cotton, R., Krämer, M., Mangold, A., and Heymsfield, A. J.: Efficiency of the deposition mode ice nucleation on mineral dust particles, Atmospheric Chemistry and Physics, 6, 3007–3021, https://doi.org/10.5194/acp-6-3007-2006, https://acp.copernicus.org/articles/6/3007/2006/, 2006.

Morrison, H. and Milbrandt, J. A.: Parameterization of Cloud Microphysics Based on the Prediction of Bulk Ice Particle Properties. Part I: Scheme Description and Idealized Tests, Journal of the Atmospheric Sciences, 72, 287–311, https://doi.org/10.1175/JAS-D-14-0065.1, https://doi.org/10.1175/JAS-D-14-0065.1, 2015.

Muench, S. and Lohmann, U.: Developing a Cloud Scheme With Prognostic Cloud Fraction and Two Moment Microphysics for ECHAM-HAM, Journal of Advances in Modeling Earth Systems, 12, e2019MS001 824, https://doi.org/10.1029/2019MS001824, https://agupubs.onlinelibrary.wiley.com/doi/abs/10.1029/2019MS001824, e2019MS001824 2019MS001824, 2020.

Muri, H., Kristjánsson, J. E., Storelvmo, T., and Pfeffer, M. A.: The climatic effects of modifying cirrus clouds in a climate engineering framework, Journal of Geophysical Research: Atmospheres, 119, 4174–4191, https://doi.org/10.1002/2013JD021063, https://agupubs.onlinelibrary.wiley.com/doi/abs/10.1002/2013JD021063, 2014.

Murphy, D. M.: Effect of Stratospheric Aerosols on Direct Sunlight and Implications for Concentrating Solar Power, Environ. Sci. Technol., 43, 2784–2786, https://doi.org/10.1021/es802206b, https://doi.org/10.1021/es802206b, 2009.

Murray, B. J., O'Sullivan, D., Atkinson, J. D., and Webb, M. E.: Ice nucleation by particles immersed in supercooled cloud droplets, Chem. Soc. Rev., 41, 6519–6554, https://doi.org/10.1039/C2CS35200A, http://dx.doi.org/10.1039/C2CS35200A, 2012.

Myhre, G., Myhre, C. L., Forster, P. M., and Shine, K. P.: Halfway to doubling of CO2 radiative forcing, Nature Geoscience, 10, 710–711, https://doi.org/10.1038/ngeo3036, https://doi.org/10.1038/ngeo3036, 2017.

Möhler, O., Benz, S., Saathoff, H., Schnaiter, M., Wagner, R., Schneider, J., Walter, S., Ebert, V., and Wagner, S.: The effect of organic coating on the heterogeneous ice nucleation efficiency of mineral dust aerosols, Environmental Research Letters, 3, 025 007, https://doi.org/10.1088/1748-9326/3/2/025007, https://doi.org/10.1088/1748-9326/3/2/025007, 2008.

Neubauer, D., Lohmann, U., Hoose, C., and Frontoso, M. G.: Impact of the representation of marine stratocumulus clouds on the anthropogenic aerosol effect, Atmospheric Chemistry and Physics, 14, 11 997–12 022, https://doi.org/10.5194/acp-14-11997-2014, https://www.atmos-chem-phys.net/14/11997/2014/, 2014.

Neubauer, D., Ferrachat, S., Siegenthaler-Le Drian, C., Stier, P., Partridge, D. G., Tegen, I., Bey, I., Stanelle, T., Kokkola, H., and Lohmann, U.: The global aerosol–climate model ECHAM6.3–HAM2.3 – Part 2: Cloud evaluation, aerosol radiative forcing, and climate sensitivity, Geoscientific Model Development, 12, 3609–3639, https://doi.org/10.5194/gmd-12-3609-2019, https://gmd.copernicus.org/articles/12/3609/2019/, 2019.

Penner, J. E., Zhou, C., and Liu, X.: Can cirrus cloud seeding be used for geoengineering?, Geophysical Research Letters, 42, 8775–8782, https://doi.org/10.1002/2015GL065992, https://agupubs.onlinelibrary.wiley.com/doi/abs/10.1002/2015GL065992, 2015.

Rind, D. and Lonergan, P.: Modeled impacts of stratospheric ozone and water vapor perturbations with implications for high-speed civil transport aircraft, Journal of Geophysical Research: Atmospheres, 100, 7381–7396, https://doi.org/https://doi.org/10.1029/95JD00196, https://agupubs.onlinelibrary.wiley.com/doi/abs/10.1029/95JD00196, 1995.

Rind, D., Lerner, J., and McLinden, C.: Changes of tracer distributions in the doubled CO2 climate, Journal of Geophysical Research: Atmospheres, 106, 28 061–28 079, https://doi.org/https://doi.org/10.1029/2001JD000439, https://agupubs.onlinelibrary.wiley.com/doi/abs/10.1029/2001JD000439, 2001.

Robock, A.: Volcanic eruptions and climate, Reviews of Geophysics, 38, 191–219, https://doi.org/https://doi.org/10.1029/1998RG000054, https://agupubs.onlinelibrary.wiley.com/doi/abs/10.1029/1998RG000054, 2000.

Robock, A., Jerch, K., and Bunzl, M.: 20 reasons why geoengineering may be a bad idea, Bulletin of the Atomic Scientists, 64, 14–59, https://doi.org/10.1080/00963402.2008.11461140, https://doi.org/10.1080/00963402.2008.11461140, 2008.

Spichtinger, P. and Cziczo, D. J.: Impact of heterogeneous ice nuclei on homogeneous freezing events in cirrus clouds, Journal of Geophysical Research: Atmospheres, 115, https://doi.org/https://doi.org/10.1029/2009JD012168, https://agupubs.onlinelibrary.wiley.com/doi/abs/10.1029/2009JD012168, 2010.

Stephens, G. L., Tsay, S.-C., Stackhouse, P. W., and Flatau, P. J.: The Relevance of the Microphysical and Radiative Properties of Cirrus Clouds to Climate and Climatic Feedback, Journal of Atmospheric Sciences, 47, 1742 – 1754, https://doi.org/10.1175/1520-0469(1990)047<1742:TROTMA>2.0.CO;2, https://journals.ametsoc.org/view/journals/atsc/47/14/1520-0469_1990_047_1742_trotma_2_0_co_2.xml, 1990.

Stevens, B., Giorgetta, M., Esch, M., Mauritsen, T., Crueger, T., Rast, S., Salzmann, M., Schmidt, H., Bader, J., Block, K., Brokopf, R., Fast, I., Kinne, S., Kornblueh, L., Lohmann, U., Pincus, R., Reichler, T., and Roeckner, E.: Atmospheric component of the MPI-M Earth System Model: ECHAM6, Journal of Advances in Modeling Earth Systems, 5, 146–172, https://doi.org/10.1002/jame.20015, https://agupubs.onlinelibrary.wiley.com/doi/abs/10.1002/jame.20015, 2013.

Stier, P., Feichter, J., Kinne, S., Kloster, S., Vignati, E., Wilson, J., Ganzeveld, L., Tegen, I., Werner, M., Balkanski, Y., Schulz, M., Boucher, O., Minikin, A., and Petzold, A.: The aerosol-climate model ECHAM5-HAM, Atmospheric Chemistry and Physics, 5, 1125–1156, https://doi.org/10.5194/acp-5-1125-2005, https://www.atmos-chem-phys.net/5/1125/2005/, 2005.

Storelvmo, T. and Herger, N.: Cirrus cloud susceptibility to the injection of ice nuclei in the upper troposphere, Journal of Geophysical Research: Atmospheres, 119, 2375–2389, https://doi.org/10.1002/2013JD020816, https://agupubs.onlinelibrary.wiley.com/doi/abs/10.1002/2013JD020816, 2014.

Storelvmo, T., Kristjansson, J. E., Muri, H., Pfeffer, M., Barahona, D., and Nenes, A.: Cirrus cloud seeding has potential to cool climate, Geophysical Research Letters, 40, 178–182, https://doi.org/10.1029/2012GL054201, https://agupubs.onlinelibrary.wiley.com/doi/abs/10.1029/2012GL054201, 2013.

Storelvmo, T., Boos, W. R., and Herger, N.: Cirrus cloud seeding: a climate engineering mechanism with reduced side effects?, Philosophical Transactions of the Royal Society A: Mathematical, Physical and Engineering Sciences, 372, 20140 116, https://doi.org/10.1098/rsta.2014.0116, https://royalsocietypublishing.org/doi/abs/10.1098/rsta.2014.0116, 2014.

Sundqvist, H., Berge, E., and Kristjánsson, J. E.: Condensation and Cloud Parameterization Studies with a Mesoscale Numerical Weather Prediction Model, Monthly Weather Review, 117, 1641–1657, https://doi.org/10.1175/1520-0493(1989)117<1641:CACPSW>2.0.CO;2, https://doi.org/10.1175/1520-0493(1989)117<1641:CACPSW>2.0.CO;2, 1989.

Tegen, I., Neubauer, D., Ferrachat, S., Siegenthaler-Le Drian, C., Bey, I., Schutgens, N., Stier, P., Watson-Parris, D., Stanelle, T., Schmidt, H., Rast, S., Kokkola, H., Schultz, M., Schroeder, S., Daskalakis, N., Barthel, S., Heinold, B., and Lohmann, U.: The global aerosol–climate model ECHAM6.3–HAM2.3 – Part 1: Aerosol evaluation, Geoscientific Model Development, 12, 1643–1677, https://doi.org/10.5194/gmd-12-1643-2019, https://gmd.copernicus.org/articles/12/1643/2019/, 2019.

Tully, C., Neubauer, D., Omanovic, N., and Lohmann, U.: Data for the "Cirrus cloud thinning using a more physically-based ice microphysics scheme in the ECHAM-HAM GCM" manuscript, https://doi.org/10.5281/zenodo.5091786, https://doi.org/10.5281/zenodo.5091786, 2021a.

Tully, C., Neubauer, D., Omanovic, N., and Lohmann, U.: Data analysis and plotting scripts for the "Cirrus cloud thinning using a more physically-based ice microphysics scheme in the ECHAM-HAM GCM" manuscript, https://doi.org/10.5281/zenodo.5091772, https://doi.org/10.5281/zenodo.5091772, 2021b.

Ullrich, R., Hoose, C., M?hler, O., Niemand, M., Wagner, R., H?hler, K., Hiranuma, N., Saathoff, H., and Leisner, T.: A New Ice Nucleation Active Site Parameterization for Desert Dust and Soot, Journal of the Atmospheric Sciences, 74, 699 – 717, https://doi.org/10.1175/JAS-D-16-0074.1, https://journals.ametsoc.org/view/journals/atsc/74/3/jas-d-16-0074.1.xml, 2017.

van Marle, M. J. E., Kloster, S., Magi, B. I., Marlon, J. R., Daniau, A.-L., Field, R. D., Arneth, A., Forrest, M., Hantson, S., Kehrwald, N. M., Knorr, W., Lasslop, G., Li, F., Mangeon, S., Yue, C., Kaiser, J. W., and van der Werf, G. R.: Historic global biomass burning emissions for CMIP6 (BB4CMIP) based on merging satellite observations with proxies and fire models (1750–2015), Geoscientific Model Development, 10, 3329–3357, https://doi.org/10.5194/gmd-10-3329-2017, https://gmd.copernicus.org/articles/10/3329/2017/, 2017.

Vaughan, N. E. and Lenton, T. M.: A review of climate geoengineering proposals, Climate Change, 109, 745–790, https://doi.org/10.1007/s10584-011-0027-7, https://doi.org/10.1007/s10584-011-0027-7, 2011.

Villanueva, D., Neubauer, D., Gasparini, B., Ickes, L., and Tegen, I.: Constraining the Impact of Dust-Driven Droplet Freezing on Climate Using Cloud-Top-Phase Observations, Geophysical Research Letters, 48, e2021GL092 687, https://doi.org/https://doi.org/10.1029/2021GL092687, https://agupubs.onlinelibrary.wiley.com/doi/abs/10.1029/2021GL092687, e2021GL092687 2021GL092687, 2021.

Wilks, D. S.: "The Stippling Shows Statistically Significant Grid Points": How Research Results are Routinely Overstated and Overinterpreted, and What to Do about It, Bulletin of the American Meteorological Society, 97, 2263 – 2273, https://doi.org/10.1175/BAMS-D-15-00267.1, https://journals.ametsoc.org/view/journals/bams/97/12/bams-d-15-00267.1.xml, 2016.

Zhang, K., O'Donnell, D., Kazil, J., Stier, P., Kinne, S., Lohmann, U., Ferrachat, S., Croft, B., Quaas, J., Wan, H., Rast, S., and Feichter, J.: The global aerosol-climate model ECHAM-HAM, version 2: sensitivity to improvements in process representations, Atmospheric Chemistry and Physics, 12, 8911–8949, https://doi.org/10.5194/acp-12-8911-2012, https://www.atmos-chem-phys.net/12/8911/2012/, 2012.